electronics

MDPI

Article

Extension-Difference-Mapping-Based PMBM Filter for Non-Ellipsoidal Extended Target Tracking

Ye Xu [1], Peng Li [2,*], Wenhui Wang [2], Youpeng Sun [1], Jiajun Ding [2] and Wenqi Geng [2]

[1] School of Mechanical Engineering, Jiangsu University of Technology, Changzhou 213000, China; noctiscoulomb@163.com (Y.X.); spyspy60@163.com (Y.S.)
[2] School of Computer Engineering, Jiangsu University of Technology, Changzhou 213000, China; wangwenhui@jsut.edu.cn (W.W.); 17315133463@163.com (J.D.); qy17638992113@163.com (W.G.)
* Correspondence: 2018500030@jsut.edu.cn

Abstract

Extended target tracking requires both accurate shape representation and efficient recursive estimation. In non-ellipsoidal extended target tracking, ellipsoidal random-matrix models are computationally efficient and suitable for Bayesian recursion, but they mainly describe the overall spatial dispersion of measurements and cannot represent local contour variations such as protrusions and concavities. In contrast, non-ellipsoidal contour models provide stronger shape representation but usually introduce higher computational complexity and stronger prior assumptions. To address this trade-off, this paper proposes an extension-difference-mapping-based Poisson multi-Bernoulli mixture filter, termed EDM-PMBM, for non-ellipsoidal extended target tracking. First, each local Bernoulli component carries a Fourier-based contour estimate and an ellipsoidal baseline propagated from the previous posterior. At the current scan, the predicted EDM function is used to map each candidate measurement subset into the EDM domain, where the EDM-induced GGIW likelihood is evaluated for PMBM data association. After the association is determined, the assigned measurement subset is used to update the posterior contour, the EDM ratio, and the EDM-domain state. The updated EDM information is then propagated to subsequent scans. In this way, shape differences are introduced into likelihood evaluation and data association without changing the basic recursive structure of the PMBM filter. Simulation results in two scenarios show that the proposed EDM-PMBM filter achieves lower GOSPA error than the compared filters and maintains more stable tracks in dense crossing situations. These results indicate that the proposed method improves the discrimination ability for non-ellipsoidal extended targets.

Keywords: extended target tracking; random matrix; multi-target tracking; Poisson multi-Bernoulli mixture; extension difference mapping

Check for updates

Academic Editor: Stefanos Kollias

Received: 23 May 2026
Revised: 16 June 2026
Accepted: 24 June 2026
Published: 26 June 2026

Copyright: © 2026 by the authors. Licensee MDPI, Basel, Switzerland. This article is an open access article distributed under the terms and conditions of the Creative Commons Attribution (CC BY) license.

1. Introduction

Multi-object tracking (MOT) is a prominent topic in both military and civilian fields [1,2]. In early MOT research, due to limited sensor resolution or small object sizes, objects were often simplified as point objects that contained only kinematic information such as position and velocity. Object sets were represented by Random Finite Sets (RFS) [3,4], leading to filters including the Probability Hypothesis Density (PHD) filter [5–7] and the Cardinalized Probability Hypothesis Density (CPHD) filter [8]. To address data association, the labeled multi-Bernoulli filter (GLMB) assigns unique labels to targets [9].

The Poisson multi-Bernoulli mixture (PMBM) filter models undetected targets as a Poisson point process (PPP) and detected targets as a multi-Bernoulli mixture (MBM), jointly handling target birth, missed detections, and recursive updates, exhibiting strong adaptability under complex measurement distributions and high clutter [10,11]. Consequently, PMBM has become an important approach in multi-target tracking. For unresolved group objects, the UO-PMBM method was developed using the UO likelihood and probability generating functional [12]. RFS theory has been combined with graph-optimized SLAM for joint data association and batch SLAM via PMBM density sampling [13]. For point/extended targets with type conversion (PETC), a hybrid PMBM method unifies Gaussian densities for point targets and Gamma Gaussian inverse-Wishart (GGIW) densities for extended targets, improving continuous tracking during type conversion [14]. A Possibility–PMBM distribution and its filtering recursion have also been defined, along with a lower-complexity Possibility–PMB approximation [15].

In the PMBM filter, shape characteristics are described by the extended state model. Existing modeling methods fall into two categories: basic geometric approximations (i.e., lines, ellipses, triangles) and complex irregular shape descriptions (i.e., multi-ellipse or parametric contours) [16]. Among basic shapes, the random-matrix (RM) model represents the target extent as a symmetric positive definite random matrix, approximates the shape as an ellipse, and recursively updates the parameters using Kalman filtering for joint kinematic and extended state estimation [16]. Subsequent Gamma inverse-Wishart (GIW) and GGIW formulations use a Gamma distribution for the measurement rate, a Gaussian distribution for kinematics, and an inverse-Wishart distribution for the shape matrix [17,18]. The RM model features a clear structure and recursive closure, making it suitable for scenarios where a single ellipse is a good approximation [19,20]. Triangles have also been used, providing few parameters and a clear structure for oriented targets or as an approximation basis [21]. However, significant shape deviation leads to model mismatch, which has motivated irregular shape modeling [22].

For irregular shapes, the multi-ellipse approximation uses multiple sub-ellipses but requires a predetermined number of ellipses. A variable-number sub-target variational Bayesian (VB) adaptive filtering method, incorporating sub-target generation and merging, VB, and an adaptive forgetting factor, jointly estimates kinematic state, extended state, mixture probabilities, and measurement noise covariance [22]. Another line improves contour description: the random hypersurface model (RHM) represents the target boundary as a parametric curve; for star-convex targets, the boundary is expanded in Fourier series, offering greater flexibility than RM but requiring pre-specified constraints and higher computational cost [23]. The Gaussian surface matrix (GSM) was introduced into RFS theory, yielding the Bayesian recursion of the GSM-PHD filter with a Gaussian mixture closed-form solution [24]. Additionally, B-spline curves from computer graphics have been combined with the RFS filter to fit arbitrary shapes via control points, though performance is sensitive to the number and distribution of control points [25].

Overall, existing extended target shape modeling methods inevitably involve a trade-off between representation capability and computational efficiency: the ellipsoidal random-matrix model is computationally efficient and recursive but has limited shape expressiveness, whereas non-ellipsoidal contour modeling methods offer stronger representational power but usually incur higher computational complexity and rely on stronger priors. Therefore, introducing effective shape discrimination information while retaining the recursive efficiency of the ellipsoidal model remains an important research problem.

To address this issue, this paper proposes an extension-difference-mapping-based PMBM filter for non-ellipsoidal extended target tracking. The main idea is to convert direction-dependent contour differences into an auxiliary EDM-domain extension represen-

tation, so that irregular shape information can participate in likelihood evaluation while the original GGIW-PMBM recursion is retained.

Unlike the random hypersurface model (RHM) [23] which directly incorporates shape parameters (e.g., Fourier coefficients) into the target state and modifies the measurement equation, our EDM approach retains the original ellipsoidal GGIW recursion. RHM offers high shape fidelity but at the cost of increased computational complexity and the need to redesign the filter update. In contrast, EDM introduces shape information only via a pre-update radial mapping function, leaving the core GGIW-PMBM recursion unchanged. This distinction makes EDM computationally lighter, easier to integrate into existing ellipsoidal-based trackers, and more robust in dense crossing scenarios.

This work contributes to non-ellipsoidal extended target tracking through four incremental steps, each detailed in a dedicated section. Section 2.3 establishes a radar measurement model for irregularly shaped targets, linking the true target contour to the spatial distribution of measurements. Section 3 designs an angular partitioning and Fourier-series-based method to update irregular contour parameters from measurement subsets after association. Section 4 proposes extension difference mapping (EDM), which uses the predicted direction-dependent ratio between the irregular contour and the ellipsoidal baseline to construct a radial scaling function for current association. Section 4.3 embeds the EDM-GGIW recursion into the PMBM multi-target filter and separates two operations: prior EDM likelihood evaluation for data association and posterior EDM shape update after association. Section 5 validates through simulations that the proposed EDM-PMBM filter outperforms existing methods in missed detections, localization, and shape accuracy while preserving ellipsoidal computational efficiency.

The proposed EDM-PMBM filter for non-ellipsoidal extended object tracking is fully implemented and the source code is publicly available at https://github.com/OmegaEta/EDM.git (accessed on 22 June 2026).

2. Background and Problem Formulation

2.1. Poisson Multi-Bernoulli Mixture Filter

The Poisson multi-Bernoulli mixture (PMBM) filter recursively propagates a multi-target posterior that always maintains the PMBM density. The posterior consists of a Poisson point process (PPP) for undetected targets and a multi-Bernoulli mixture (MBM) for detected targets.

Let the updated PMBM posterior at time k be expressed as

$$D_k(\cdot) \cup \left\{ \left(W_k^j \middle| \left\{ r_k^{j,i}, f_k^{j,i}(\cdot) \right\}_{i \in \mathbb{I}^j} \right) \right\}_{j \in \mathbb{J}_k}, \tag{1}$$

where $D_k(\cdot)$ is the PPP intensity for undetected targets, $\mathbb{J}_k$ is the set of global hypotheses, $\mathbb{I}_j$ indexes Bernoulli components under the j-th global hypothesis, W_k^j is the hypothesis weight, and $r_k^{j,i}$ and $f_k^{j,i}(\cdot)$ are the existence probability and single-target density of a Bernoulli component.

PMBM Prediction: The predicted PMBM density at time $k+1$ is obtained by propagating the PPP and MBM components through the target dynamics.

$$D_{k+1|k}(x_{k+1}) = D_{k+1}^b(x_{k+1}) + \int p_S(x_k) f_{k+1|k}(x_{k+1} \mid x_k) D_k(x_k) dx_k, \tag{2}$$

$$W_{k+1|k}^j = W_k^j, \tag{3}$$

$$r_{k+1|k}^{j,i} = r_k^{j,i} \int p_S(x_k) f_k^{j,i}(x_k) dx_k, \tag{4}$$

$$f_{k+1|k}^{j,i}(x_{k+1}) = \frac{\int p_S(x_k) f_{k+1|k}(x_{k+1} \mid x_k) f_k^{j,i}(x_k) dx_k}{\int p_S(x_k) f_k^{j,i}(x_k) dx_k}, \tag{5}$$

Here, $D_{k+1}^b(\cdot)$ is the PPP intensity of newborn targets, $p_S(\cdot)$ the survival probability, and $f_{k+1|k}(\cdot \mid \cdot)$ the single-target transition density.

PMBM Update: Upon receiving measurement set Z_{k+1}, the updated PMBM posterior is obtained by considering all feasible associations between measurements and existing Bernoulli components or new targets from the PPP.

$$D_{k+1}(\cdot) \cup \left\{ \left(W_{k+1}^{j,A} \middle| \left\{ r_{k+1}^{j,A,C}, f_{k+1}^{j,A,C}(\cdot) \right\}_{C \in A} \right) \right\}_{j \in \mathbb{J}_k, A \in \mathcal{A}_j}, \tag{6}$$

where $\mathcal{A}_j$ is the set of feasible association hypotheses under global hypothesis j, and $A \in \mathcal{A}_j$ is a specific association. Each association $C \in A$ corresponds to either an existing Bernoulli component or a new target generated from the PPP.

The PPP intensity is updated as

$$D_{k+1}(x_{k+1}) = q_D(x_{k+1}) D_{k+1|k}(x_{k+1}), \tag{7}$$

$$q_D(x_{k+1}) = 1 - p_D(x_{k+1}) + p_D(x_{k+1}) e^{-\gamma(x_{k+1})}, \tag{8}$$

where $p_D(\cdot)$ is the detection probability, $\gamma(\cdot)$ the Poisson measurement rate of an extended target, and $q_D(\cdot)$ the probability that the target is not detected or detected but produces no measurements.

2.2. Ellipsoidal Extended State Modeling

The description of symbols related to the measurement model for irregularly shaped extended targets is given in Table 1.

Table 1. Description of symbols related to the measurement model for extended state modeling.

Index	Symbol	Description
2	x	target state, with $x = \{\gamma, \xi, X\}$
3	X	ellipsoidal extended state matrix, with $X = \{\nu, V\}$
4	ν	degrees-of-freedom parameter of the inverse-Wishart distribution
5	V	scale parameter of the inverse-Wishart distribution
6	$\mathcal{IW}(X; \nu, V)$	the extended state matrix X follows an inverse-Wishart distribution

Let the center of the i-th target at time k be $m_k^i \in \mathbb{R}^2$, and let its ellipsoidal extension state be represented by a symmetric positive definite matrix $X_k^i \in \mathbb{S}_{++}^2$. The corresponding ellipsoidal boundary can then be expressed as

$$(y - m_k^i)^T (X_k^i)^{-1} (y - m_k^i) = 1, \tag{9}$$

where $y \in \mathbb{R}^2$ denotes a point on the ellipsoidal boundary in the plane, and $\mathbb{S}_{++}^2$ denotes the space of 2×2 symmetric positive definite matrices.

Let the true shape-constrained region corresponding to the target state x_k^i be $C(x_k^i)$, and let its ellipsoidal approximation be denoted by $C_e(x_k^i)$. Then the region occupied by this ellipsoidal extension can be expressed as

$$C_e(x_k^i) = \left\{ y \in \mathbb{R}^2 : (y - m_k^i)^T (X_k^i)^{-1} (y - m_k^i) \leq 1 \right\}. \tag{10}$$

To provide a more intuitive illustration of the geometric meaning of the ellipsoidal extension state, the extension state matrix X_k^i can be decomposed as

$$X_k^i = \mathrm{Rot}\left(\alpha_k^i\right)\begin{bmatrix}\left(\lambda_{k,1}^i\right)^2 & 0\\ 0 & \left(\lambda_{k,2}^i\right)^2\end{bmatrix}\mathrm{Rot}^T\left(\alpha_k^i\right), \tag{11}$$

$$\mathrm{Rot}\left(\alpha_k^i\right) = \begin{bmatrix}\cos\alpha_k^i & -\sin\alpha_k^i\\ \sin\alpha_k^i & \cos\alpha_k^i\end{bmatrix}. \tag{12}$$

where α_k^i denotes the orientation angle of the ellipsoidal principal axis, and $\lambda_{k,1}^i$ and $\lambda_{k,2}^i$ denote the lengths of the two semi-axes, respectively. From the above expressions, the ellipsoidal extension state essentially captures the overall dispersion range, the principal extension direction, and the major and minor axis scales of the target measurements in space. In other words, within the ellipsoidal model filter, a complex target contour is compressed into a quadratic region jointly determined by the center, orientation, and axis lengths.

In the random-matrix approach, the extension matrix X_k^i in (11) is typically modeled as an $\mathcal{IW}$ distribution,

$$X_k^i \sim \mathcal{IW}\left(\nu_k^i, V_k^i\right), \tag{13}$$

whose probability density function is given by

$$\mathcal{IW}\left(X_k^i; \nu_k^i, V_k^i\right) = \frac{2^{\frac{(\nu_k^i-d-1)d}{2}}\left|V_k^i\right|^{\frac{\nu_k^i-d-1}{2}}}{\Gamma_d\left(\frac{\nu_k^i-d-1}{2}\right)\left|X_k^i\right|^{-\frac{\nu_k^i}{2}}}\mathrm{etr}\left(-\frac{1}{2}V_k^i{X_k^i}^{-1}\right), \tag{14}$$

where $d \in \mathbb{N}_+$ denotes the matrix dimension, ν_k^i is the degrees-of-freedom parameter, $V_k^i \in \mathbb{S}_{++}^d$ is the scale matrix, $\Gamma_d(\cdot)$ denotes the multivariate Gamma function, and $\mathrm{etr}\left(\cdot\right) = \exp\left(\mathrm{tr}(\cdot)\right)$.

The inverse-Wishart distribution is conjugate to the Gaussian likelihood for the measurement covariance, which enables closed-form recursive updates within the Bayesian filtering framework. This conjugacy property, together with the positive definiteness constraint naturally enforced by the $\mathcal{IW}$ distribution, makes it particularly suitable for random-matrix-based extended target tracking.

2.3. Problem Formulation

2.3.1. Measurement Model for Irregularly Shaped Extended Targets

To model irregularly shaped extended targets, one must first define their measurement model and then describe the extended target state via the measurement distribution and the kinematic state. Rather than directly assuming that the measurement points are distributed around a given contour, the measurement model is established by considering the generation process of the echo source points originating from the target shape.

The description of symbols related to the measurement model for irregularly shaped extended targets is given in Table 2.

The uniform model is adopted here to provide a tractable connection between the target region $C(x_k)$, the measurement spatial density $\varphi(z \mid x_k)$, and the set likelihood. Similar Gaussian-noise-based measurement assumptions are widely used in random-matrix and GGIW extended target tracking models [16,18], while the PMBM association recursion follows the standard implementation in [10].

Let the true shape-constrained region corresponding to the target state x_k be $C(x_k)$. This region is uniquely determined by the shape parameters of the target and can be any non-ellipsoidal closed region. Based on the above setting, the following assumptions are made:

Table 2. Description of symbols related to the measurement model for irregularly shaped extended targets.

Index	Symbol	Description
1	z	single extended target measurement
2	Z	extended target measurement set
3	s	noise-free echo source point
4	$\mathcal{U}(\cdot)$	defined uniform distribution
5	$\mathcal{N}(\mathcal{E}, \sigma)$	Gaussian noise with mean $\mathcal{E}$ and covariance σ
6	ℓ	conditional likelihood
7	γ	measurement rate of the extended target
8	$Poisson(\cdot)$	denotes a Poisson distribution
9	$\rho_c(\theta)$	polar radius of the irregular shape at angle θ
10	$\mathcal{F}(\cdot)$	polar radius function of the irregularly shaped target
11	$\hat{C}_{c,k}$	parametric representation of the irregular shape contour
12	$\mathbb{D}$	maximum polar radius
13	$C(\cdot)$	irregular shape modeling constraint of the target
14	$C_e(\cdot)$	ellipsoidal shape modeling constraint of the target
15	$\varphi(\cdot)$	spatial distribution of measurements for irregular shape
16	$\varphi_e(\cdot)$	spatial distribution of measurements for ellipsoidal shape
17	$Cov(\cdot)$	covariance of the measurement samples
18	α_k	orientation of the ellipse major axis at time k
19	$\lambda_{k,1}$	semi-major axis length of the ellipse at time k
20	$\lambda_{k,2}$	semi-minor axis length of the ellipse at time k
21	$\Gamma_d(\cdot)$	multivariate Gamma function

Assumption 1. *After the sensor illuminates the target and receives the echoes, the true spatial occupancy region of the target can be described by the shape constraint $C(x_k)$, which denotes the true shape region of the target on the observation plane. The noise-free echo source points generated by the sensor within this region are uniformly distributed.*

Assumption 2. *The echo sources of the target are uniformly distributed within the region $C(x_k)$; that is, all locations within the region have the same probability of generating an echo.*

Assumption 3. *The sensor measurements are subject to location errors; each echo source is corrupted by Gaussian-distributed position noise before forming the final measurement.*

Under the above assumptions, if the target produces a total of n_k measurements at time k, the r-th measurement can be expressed as

$$z_k^r = s_k^r + \mathcal{N}(0, R_k), r = 1, 2, \ldots, n_k, \tag{15}$$

$$s_k^r \sim \mathcal{U}(C(x_k)), \tag{16}$$

where s_k^r denotes the noise-free echo source point, $\mathcal{N}(0, R_k)$ denotes the zero-mean Gaussian measurement noise, and R_k is the covariance matrix of the sensor measurement noise. $\mathcal{U}(C(x_k))$ denotes the uniform distribution defined on the region $C(x_k)$. The above equations show that the generation process of a single measurement can be divided into two steps: first, a noise-free echo source point is uniformly sampled within the true shape region $C(x_k)$ of the target; then, Gaussian noise is added to that source point to obtain the final sensor measurement.

Consequently, the measurement set corresponding to the target at time k can be written as

$$Z_k = \left\{ z_k^1, z_k^2, \ldots, z_k^{n_k} \right\}, \tag{17}$$

Given the target state x_k, the spatial distribution of a single measurement can be expressed as the convolution of the uniform distribution with Gaussian noise.

$$\varphi(z \mid x_k) = \int \mathcal{N}(z; s, R_k)\, \mathcal{U}(s; C(x_k))\, ds. \tag{18}$$

The spatial distribution of measurements for a non-ellipsoidal extended target is no longer determined by a simple ellipsoidal geometry, but rather by the true shape region $C(x_k)$ and the sensor noise. If the area of the region $C(x_k)$ is denoted by $|C(x_k)|$, the above expression can also be written as

$$\varphi(z \mid x_k) = \frac{1}{|C(x_k)|} \int_{s \in C(x_k)} \mathcal{N}(z; s, R_k)\, ds. \tag{19}$$

If, additionally, the number of measurements generated by the target follows a Poisson distribution,

$$n \sim \text{Poisson}(\gamma(x_k)), \tag{20}$$

where $\gamma(x_k)$ is the measurement rate associated with the target state x_k, then the conditional likelihood of the measurement set Z_k corresponding to the target can be written as

$$\ell(Z_k \mid x_k) = e^{-\gamma(x_k)} \prod_{z \in Z_k} \gamma(x_k)\, \varphi(z \mid x_k), Z_k \neq \emptyset. \tag{21}$$

2.3.2. Problem Formulation for Ellipsoidal Extended Targets

Although ellipsoidal extension modeling is widely used in extended target tracking, it has limitations when the true target shape exhibits markedly irregular boundaries. As shown in Section 3, given the target state x_k^i, the spatial distribution of a single measurement is jointly determined by the true shape region $C(x_k)$ and the sensor noise R_k (see (18) and (19)). For irregular targets with sharp corners, concavities, or local protrusions, the measurement distribution carries richer geometric information than just the overall scale and principal direction.

In ellipsoidal modeling, the target shape is approximated by an ellipsoidal region $C_e(x_k)$ with (13), where X_k is determined solely by the center, orientation, and axis lengths. Consequently, the measurement distribution becomes an approximation based on the ellipsoidal region,

$$\varphi(z \mid x_k) \approx \varphi_e(z \mid x_k) = \frac{1}{|\, C_e(x_k)\,|} \int_{s \in C_e(x_k)} \mathcal{N}(z; s, R_k)\, ds. \tag{22}$$

Compared with the true distribution $\varphi(z \mid x_k)$, $\varphi_e(z \mid x_k)$ only reflects the dispersion range and loses local boundary details. Local geometric differences are compressed or obscured, weakening the ability to represent irregular shapes.

This point is further illustrated by the decomposition of the ellipsoidal extension matrix. Let the sample means and covariances of two targets A and B be approximately equal: $z_k^A \approx z_k^B$ and $\text{Cov}(A) \approx \text{Cov}(B)$. Then, the resulting ellipsoidal extension matrices satisfy $X_k^A \approx X_k^B$. Decomposing X_k as

$$X_k = \text{Rot}\,(\alpha_k) \begin{bmatrix} \lambda_{k,1} & 0 \\ 0 & \lambda_{k,2} \end{bmatrix} \text{Rot}^T(\alpha_k), \tag{23}$$

where α_k is the orientation and $\lambda_{k,1}, \lambda_{k,2}$ the semi-axis lengths, it follows that $\alpha_k^A \approx \alpha_k^B$, $\lambda_{k,1}^A \approx \lambda_{k,1}^B$, and $\lambda_{k,2}^A \approx \lambda_{k,2}^B$. Thus, under ellipsoidal modeling, targets with different true shapes may be represented by similar ellipsoidal extensions, as illustrated in Figure 1.

In Figure 1, although the contours of object A and object B differ significantly in protrusions and concavities, their measurement means and covariances are similar, leading to nearly identical ellipsoidal extensions (yellow dashed circles of radius about 2). Hence,

ellipsoidal modeling captures the overall measurement envelope but is insensitive to direction-dependent local boundary variations.

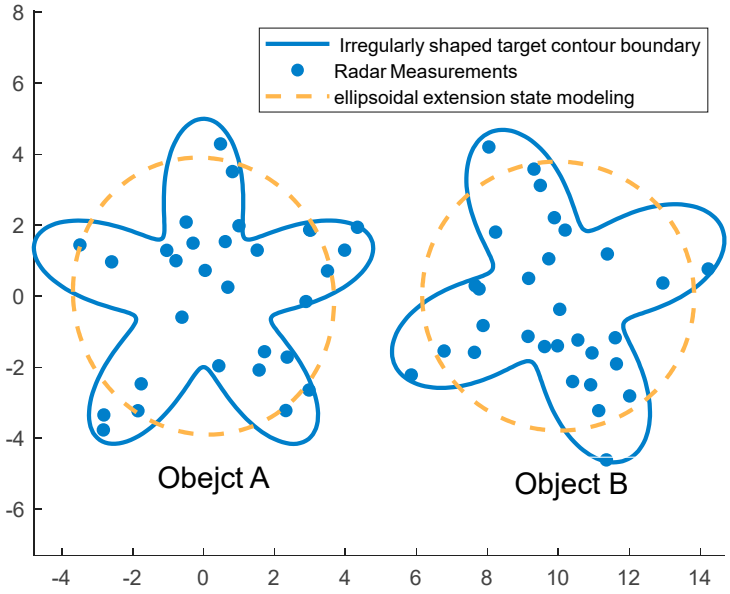


Figure 1. Similar representations of targets with different shapes under ellipsoidal modeling.

3. Irregular Shape Parameter Estimation Method

Following the limitations discussed in Section 2.3.2, this section estimates a radial contour representation from the target-associated measurement subset. The estimated contour provides the direction-dependent radial observations required for the subsequent EDM construction. A parametric representation of the true contour is therefore necessary to enable subsequent extension difference mapping. This section presents a contour estimation method for irregularly shaped targets. In Section 2.3, $C(x_k)$ denotes the true irregular contour and $C_e(x_k)$ the ellipsoidal approximation. Since $C(x_k)$ is not directly available in filtering, a measurement reconstruction method is used to obtain the irregular contour estimate $\hat{C}_{c,k}$.

Given a target-associated measurement subset, this section extracts direction-dependent radial observations and reconstructs a Fourier-based contour representation. The resulting contour parameters provide the local radial information required for the subsequent EDM construction.

The contour estimation in this section is a posterior shape-update operation applied to the assigned measurement subset after association. Instead, the updated contour is stored as posterior shape information and is propagated to the next scan.

To facilitate recursion and comparison, $\hat{C}_{c,k}$ is described in polar coordinates,

$$C(x_k) \sim \mathcal{F}(\hat{C}_{c,k}; \theta), \tag{24}$$

where $\mathcal{F}(\hat{C}_{c,k}; \theta)$ is the radial function of the true contour in direction $\theta \in [0, 2\pi)$, i.e., the distance from target center m_k to the contour boundary. A J-th order Fourier series expands this radial function, and the contour parameter vector is defined as

$$\hat{C}_{c,k} = \left(a_{0,k}, \{a_{j,k}\}_{j=1}^{J}, \{b_{j,k}\}_{j=1}^{J} \right), \tag{25}$$

with the radial function given by

$$\mathcal{F}(\hat{C}_{c,k}; \theta) = \frac{a_{0,k}}{2} + \sum_{j=1}^{J} \left(a_{j,k} \cos(j\theta) + b_{j,k} \sin(j\theta) \right). \tag{26}$$

To extract direction-dependent local extension information from the measurement set Z_k, an angular partition is constructed around the target center m_k. Define

$$\mathbb{D}_k = \max_{\theta \in [0,2\pi)} \mathcal{F}(\hat{C}_{c,k|k-1}; \theta), \tag{27}$$

as the maximum radial distance of the predicted contour. $\mathbb{D}_k$ is the radius of the circumcircle centered at m_k, providing a unified spatial scale for partitioning. If the predicted contour parameter is unavailable, $\mathbb{D}_k$ may be approximated by the maximum semi-axis length of the baseline ellipsoid $\hat{C}^i_{e,k}$.

As illustrated in Figure 2, the angular interval $[0,\ 2\pi)$ is uniformly divided into N sectors, with the center direction of the n-th sector defined as

$$\theta_n = \frac{2\pi(n-1)}{N}, n = 1, 2, \ldots, N. \tag{28}$$

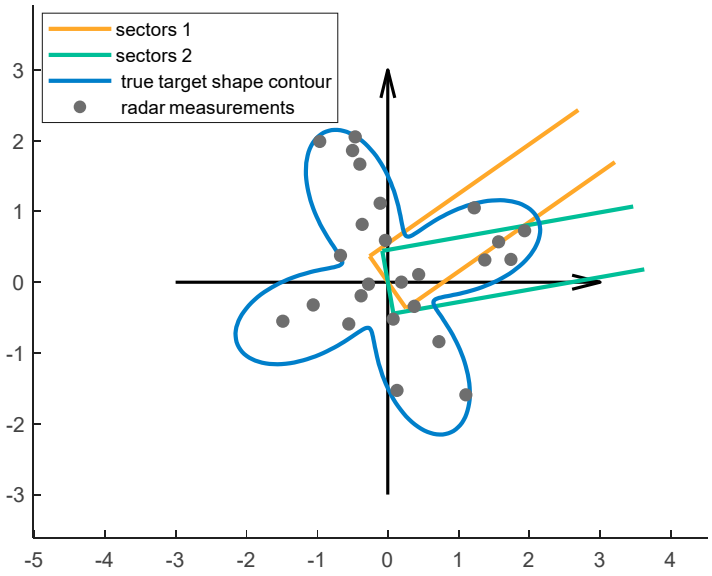


Figure 2. Illustration of angular measurement partition.

For any measurement point $z \in Z_k$, let $\delta z = z - m_k$. The forward projection Φ_2 and lateral deviation Φ_1 onto the sector center direction are

$$\begin{bmatrix} \Phi_2(z; \theta_n) \\ \Phi_1(z; \theta_n) \end{bmatrix} = R(\theta_n)(z - m_k). \tag{29}$$

The measurement subset for the n-th sector is

$$Z_{k,n} = \left\{ z \in Z_k \mid \ | \Phi_1(z; \theta_n) | \leq \mathbb{D}_k \sin\frac{\pi}{N}, \Phi_2(z; \theta_n) > 0 \right\}. \tag{30}$$

Here, $Z_{k,n}$ is the measurement subset assigned to the n-th angular sector. The condition on $\Phi_1(z; \theta_n)$ controls the lateral width of the sector, while the condition $\Phi_2(z; \theta_n) > 0$ ensures that the measurement lies in the forward direction of the sector.

Thus, the original measurement set is divided into directionally localized subsets. For each sector, the local random-matrix extension estimate is used to extract a direction-dependent radial scale. It should be noted that this step does not assume that the true local contour is exactly elliptical. Instead, the inverse-Wishart random matrix is used as a positive-definite local equivalent extension model, from which a stable directional extension length can be obtained.

For the n-th sector, the local equivalent extension matrix is modeled as

$$X_{k,n} \sim \mathcal{IW}_d(\nu_{k,n}, V_{k,n}), \tag{31}$$

where $X_{k,n} \in \mathbb{S}^d_{++}$ denotes the local equivalent extension matrix of the n-th sector, d is the measurement dimension, $\nu_{k,n}$ is the degrees-of-freedom parameter, and $V_{k,n} \in \mathbb{S}^d_{++}$ is the scale matrix. The measurements assigned to this sector provide the second-order information used to update the local extension parameters. In the random-matrix update form, the parameter update can be written as

$$\nu_{k,n} = \nu_{k|k-1,n} + \mid Z_{k,n} \mid, \tag{32}$$

$$V_{k,n} = V_{k|k-1,n} + \sum_{z \in Z_{k,n}} (z - m_k)(z - m_k)^T, \tag{33}$$

Here, $Z_{k,n}$ is the measurement subset assigned to the n-th sector, $\mid Z_{k,n} \mid$ is the number of measurements in this subset, z is a measurement point, and m_k is the estimated target centroid at time k. The summation term represents the second-order contribution of the measurements in this sector. It is used to update the scale matrix $V_{k,n}$, rather than being interpreted as an inverse-Wishart distributed random matrix.

Under the inverse-Wishart convention adopted in this paper, the local equivalent extension estimate is obtained by

$$\bar{X}_{k,n} = \frac{V_{k,n}}{\nu_{k,n} - 2d - 2} \tag{34}$$

where $\bar{X}_{k,n}$ denotes the posterior mean of the local equivalent extension matrix in the n-th sector. Since $V_{c,k,n}$ is positive definite, it defines a local equivalent ellipse. Let its eigenvalue decomposition be

$$\bar{X}_{k,n} = U_{k,n} \mathrm{diag}\,(\lambda_{1,k,n}, \lambda_{2,k,n}) U_{k,n}^T, \tag{35}$$

where $U_{k,n}$ is an orthogonal matrix, whose columns are the eigenvectors of $V_{c,k,n}$, and $\lambda_{1,k,n}$ and $\lambda_{2,k,n}$ are its eigenvalues. The quantities $\sqrt{\lambda_{1,k,n}}$ and $\sqrt{\lambda_{2,k,n}}$ correspond to the two principal semi-axis lengths of the local equivalent ellipse. Therefore, the random-matrix estimate provides a local elliptical support, whose principal axes describe the local extension scale of the measurement subset.

The direction vector of the n-th sector is

$$u_n = \left[\cos\theta_n, \sin\theta_n\right]^T, \tag{36}$$

where θ_n is the center angle of the n-th sector. The radial distance sample in this direction is then computed as

$$\rho_{c,k}(\theta_n) = \sqrt{u_n^T \bar{X}_{k,n} u_n}. \tag{37}$$

When u_n is aligned with a principal direction of $V_{c,k,n}$, this value equals the corresponding principal semi-axis length. For a general sector direction, it gives the directional extension scale of the local equivalent ellipse. Since each sector covers a narrow angular region, this directional scale is used as an approximation of the distance from the target centroid to the outer contour in direction θ_n.The radial samples $\{\rho_{c,k}(\theta_n)\}_{n=1}^N$ are then used to reconstruct the Fourier contour parameters according to Equations (38) and (40). Specifically,

$$a_{0,k} = \frac{1}{N} \sum_{n=1}^{N} \rho_{c,k}(\theta_n), \tag{38}$$

$$a_{j,k} = \frac{2}{N}\sum_{n=1}^{N}\rho_{c,k}(\theta_n)\cos(j\theta_n), j = 1,\ldots,J, \tag{39}$$

$$b_{j,k} = \frac{2}{N}\sum_{n=1}^{N}\rho_{c,k}(\theta_n)\sin(j\theta_n), j = 1,\ldots,J. \tag{40}$$

The resulting parameter vector

$$\hat{C}_{c,k} = \left(a_{0,k}, \{a_{j,k}\}_{j=1}^{J}, \{b_{j,k}\}_{j=1}^{J}\right), \tag{41}$$

defines the reconstructed irregular contour at time k. The procedure is summarized in Table 3.

Table 3. Pseudocode for local extension state and contour parameter estimation of irregularly shaped targets.

Input: original measurement subset Z_k, local shape state prior $V_{c,k-1,n}$, irregular contour prior parameter $\hat{C}_{c,k|k-1}$;
Output: local shape state posterior $V_{c,k,n}$; irregular contour posterior parameter $\hat{C}_{c,k}$;
Parameters: N is the number of sectors, with $n = 1, 2, \ldots, N$;

Partition of the original measurement subset.
  Compute the maximum polar radius $\mathbb{D}_k$ for contour partition, refer to Equation (27);
  Compute the forward projection Φ_2 and lateral deviation Φ_1 of the contour, refer to Equation (29);
  Partition the original measurement set into N measurement subsets $\{Z_{k,n}\}_{n=1}^{N}$, refer to Equation (30);
Local extension state estimation:
  for $n = 1, \ldots, N$ **do**
    Compute the local extension state $V_{c,k,n}$ for the corresponding sector; refer to Equations (31)–(33);
    Compute the discrete contour sample $\rho_{c,k}$ at the current time; refer to Equation (37);
  end for
  Reconstruct the irregular contour parameter $\hat{C}_{c,k}$ at the current time; refer to Equations (38)–(40).

4. Extension Difference Model

Before presenting the EDM construction, it is necessary to clarify the role of the radial scaling used in this paper. Although EDM also uses a direction-dependent scaling function, its purpose is different from the random scaling factor in RHM. In RHM, the scaling variable belongs to the measurement generation process and describes the possible source location of an individual measurement inside a scaled version of the target boundary. Hence, the boundary parameters are directly involved in the nonlinear measurement update.

In contrast, the EDM scaling function is constructed from the radial ratio between the irregular contour estimate and the ellipsoidal baseline. It is used to transform the measurement subset into an auxiliary EDM domain rather than to describe the physical generation position of each measurement. The subsequent likelihood comparison is performed by evaluating the consistency between the EDM-domain posterior extension and the predicted EDM-domain prior extension. Therefore, EDM introduces non-ellipsoidal shape cues into PMBM data association without replacing the original GGIW random-matrix recursion.

4.1. Key Method of Extended Difference

The purpose of EDM is to introduce direction-dependent shape information into the ellipsoidal GGIW-PMBM framework without changing its basic recursive structure. For each local Bernoulli hypothesis, the predicted irregular contour and the predicted ellipsoidal baseline are compared in polar coordinates. Their radial difference is converted into a direction-dependent scaling function, which maps a candidate measurement cell into the EDM domain. The mapped cell is then evaluated by the EDM-domain GGIW likelihood, and the resulting marginal likelihood is used in the PMBM association weight.

Therefore, EDM does not introduce an independent shape classification rule. Shape information affects data association only through the transformed-domain likelihood. The symbols used in the EDM construction are summarized in Table 4.

Table 4. Description of symbols related to the extended difference mapping method.

Index	Symbol	Description
1	H or (h)	candidate hypothesis $h = \{C_c, C_e, f_{\mathrm{EDM}}(\theta)\}$
2	z^C	the candidate measurement subset is composed in candidate hypothesis counter
3	Z	extended target measurement set
4	X	ellipsoidal extended state matrix
5	f_h	EDM function constructed from h
6	$Map(Z, f_h)$	mapping operator applied to Z using the EDM function f_h
7	Z_f	subset of measurements in the EDM domain under candidate shape hypothesis h
8	X_f	extended state matrix in the EDM domain under candidate shape hypothesis h
9	v_f	degrees-of-freedom parameter of the inverse-Wishart distribution in the EDM domain
10	V_f	scale parameter of the Wishart distribution in the EDM domain

In this paper, the candidate shape hypothesis $h_k^{j,i}$ is attached to the i-th Bernoulli component under the j-th global hypothesis, rather than selected from a predefined shape-template library. It is defined as

$$h_k^{j,i} = \left\{ \hat{C}_{c,k|k-1}^{j,i}, \hat{C}_{e,k|k-1}^{j,i}, f_{\mathrm{EDM},k|k-1}^{j,i}(\theta) \right\}, \tag{42}$$

where $\hat{C}_{c,k|k-1}^{j,i}$ is the predicted irregular contour obtained from previous recursive shape estimation, $\hat{C}_{e,k|k-1}^{j,i}$ is the predicted ellipsoidal baseline contour, and $f_{\mathrm{EDM},k|k-1}^{j,i}(\theta)$ is the predicted direction-dependent EDM radial scaling function. These quantities are not selected from an external template library, but are gradually updated from historical measurements.

The role of $h_k^{j,i}$ is to provide a shape-conditioned likelihood for measurement partition and association. When targets are well separated, the measurement-to-target association is usually dominated by spatial distance and kinematic consistency. However, when multiple extended targets are closely spaced or crossing, measurement partition becomes highly ambiguous. In this case, the candidate shape hypotheses propagated from previous time steps provide additional contour information. For a possible measurement subset Z_C, the EDM mapping constructed from $h_k^{j,i}$ maps Z_C into the EDM domain, and the resulting EDM-domain likelihood evaluates whether this subset is consistent with the previously estimated target contour. Thus, the measurement subset with higher shape consistency obtains a larger likelihood.

Therefore, the number of candidate shape hypotheses is not determined by a shape-template library. It is determined by the number of local target hypotheses involved in the current ambiguous association region. In closely spaced or crossing scenarios, the candidate shape hypotheses correspond to the previously estimated contours of the neighboring targets. The filter does not enumerate multiple independent Fourier parameter vectors for the same target. Instead, different candidate shapes arise from different local target hypotheses maintained by the PMBM recursion.

With this clarification, for each candidate shape hypothesis $h_k^{j,i}$, a corresponding EDM function f_h can be constructed from the angular scale difference between the predicted irregular contour and its predicted ellipsoidal baseline. After applying the EDM mapping

associated with $h_k^{j,i}$ to a possible measurement subset Z_C, the mapped measurement set in the EDM domain is

$$Z_{f,k}^{C,(h)} = \mathrm{Map}(Z_C, f_h), \tag{43}$$

The likelihood computed from $Z_{f,k}^{C,(h)}$ is then used to evaluate the shape consistency between the candidate measurement subset and the historical target contour represented by $h_k^{j,i}$.

Let the original measurement subset of a target at time k be Z_k^i. For each candidate shape hypothesis h, a corresponding EDM function f_h can be constructed. This function is determined by the angular scale difference between the candidate shape contour and its baseline ellipsoid; it is essentially a direction-dependent radial scaling function. After applying the EDM mapping of candidate shape hypothesis h to the original measurement subset Z_k^i, the measurement set in the EDM domain is

$$Z_{f,k}^{i,(h)} = \mathrm{Map}\left(Z_k^i, f_h\right), \tag{44}$$

where $\mathrm{Map}(\cdot)$ denotes the radial mapping operator induced by the EDM function. This operator keeps the angle of each measurement point relative to the target center unchanged and only adjusts the radial position according to the scale differences in the candidate shape in various directions.

After obtaining the EDM-domain measurement set $Z_{f,k}^{i,(h)}$, it serves as the observation basis for the EDM-domain extension state, and the EDM-domain extension state parameters can be further updated, yielding the corresponding EDM-domain ellipsoidal extension estimate

$$X_{f,k}^{i,(h)} \sim \mathcal{IW}_d\left(\nu_{f,k}^{i,(h)}, V_{f,k}^{i,(h)}\right). \tag{45}$$

Consequently, the mean of the equivalent extension state in the EDM domain corresponding to this candidate shape is

$$\bar{X}_{f,k}^{i,(h)} = \mathbb{E}\left[X_{f,k}^{i,(h)}\right] = \frac{V_{f,k}^{i,(h)}}{\nu_{f,k}^{i,(h)} - 2d - 2}. \tag{46}$$

On the other hand, the EDM-domain extension state obtained at the previous time step can be propagated to the current time according to the prediction relation of the random-matrix model, giving the EDM-domain prior extension state

$$X_{f,k|k-1}^{i,(h)} = M\left(\xi_{k-1}^i\right) X_{f,k-1}^{i,(h)} M^{\mathrm{T}}\left(\xi_{k-1}^i\right). \tag{47}$$

For the same original measurement subset Z_k^i, different local shape hypotheses h produce different EDM mapping results $Z_{f,k}^{i,(h)}$, and further yield different EDM-domain posterior extension parameters. If a shape hypothesis is close to the true target contour, the EDM mapping induced by this hypothesis makes the mapped measurement set more compatible with the predicted EDM-domain extension. Conversely, if the shape hypothesis deviates significantly from the true contour, the corresponding EDM mapping produces inappropriate angular-radial scaling, and the mapped measurement statistics become less compatible with the predicted EDM-domain extension.

The likelihood used for association is the EDM-domain marginal likelihood

$$\ell_h(Z_C) = \left[\prod_{z \in Z_C} |J_h(z)|\right] \int \ell_f\left(Z_{f,C}^{(h)} \mid x_f\right) p\left(x_f; \zeta_{f,k|k-1}^h\right) dx_f, \tag{48}$$

where $p(x_f;\zeta^h_{f,k|k-1})$ is the predicted EDM-domain GGIW density, $\ell_f(\cdot)$ is the EDM-domain extended-target likelihood, and $|\ J_h(z)\ |$ is the Jacobian determinant of the EDM transformation. Therefore, the consistency discussed here is reflected in the value of $\ell_h(Z_C)$: a mapped measurement subset that is more compatible with the predicted EDM-domain state gives a larger marginal likelihood and hence a larger association weight.

For interpretation, the compatibility between the predicted EDM-domain extension and the extension induced by the mapped measurements can be described by the following log_det_h discrepancy:

$$log_det_h = tr\left[\left(\bar{X}^h_{f,k|k-1}\right)^{-1}\bar{X}^h_{f,k}\right] - log\left|\left(\bar{X}^h_{f,k|k-1}\right)^{-1}\bar{X}^h_{f,k}\right| - d, \tag{49}$$

where $\bar{X}^h_{f,k|k-1}$ is the predicted EDM-domain extension mean, $\bar{X}^h_{f,k}$ is the posterior EDM-domain extension mean induced by the mapped measurement subset under shape hypothesis h, and d is the measurement dimension. The discrepancy log_det_h is non-negative and reaches its minimum when the two extension matrices are equal. Thus, a smaller $\mathrm{log_det}_h$ indicates a higher compatibility between the predicted extension and the mapped-measurement-induced extension.

Under the GGIW random-matrix likelihood, mismatch between the predicted extension and the mapped measurement scatter is reflected through trace and log-determinant terms. Therefore, when the measurement number, measurement rate term, and kinematic innovation are comparable, a smaller extension discrepancy log_det_h corresponds to a larger extension-related likelihood contribution. This provides a principled likelihood-related explanation for the consistency shown in Figure 3.

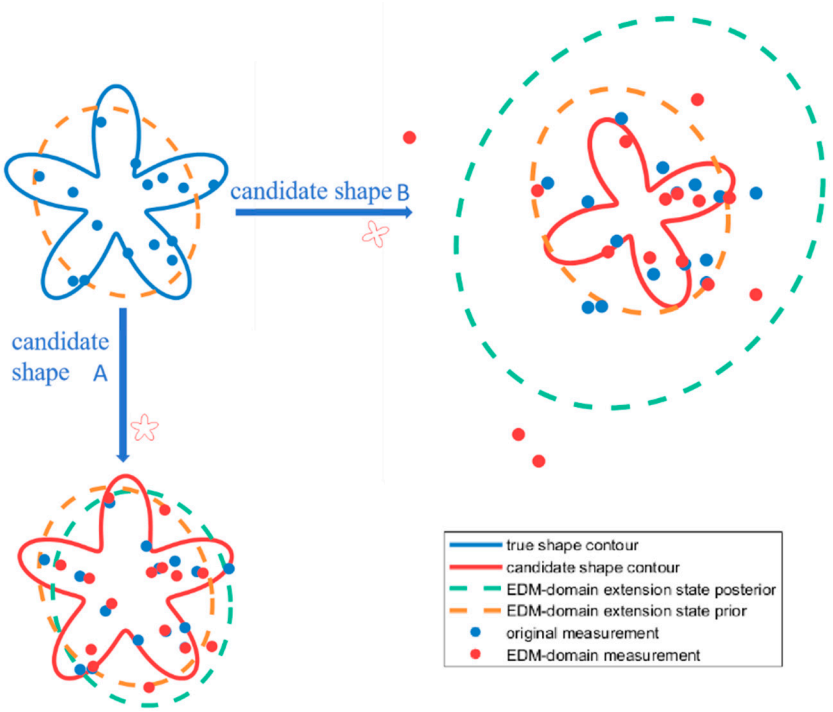


Figure 3. EDM domain differences of a target under two shape hypotheses.

Take Figure 3 as an example. Suppose the true target contour is shown by the blue solid line in the upper left, and the two local shape hypotheses correspond to shape A and shape B. Since shape A is closer to the true target contour, the mapped posterior extension $V^{i,(A)}_{f,k}$ is closer to the predicted EDM-domain extension $V^{i,(A)}_{f,k|k-1}$, which corresponds to a smaller extension discrepancy and a larger EDM-domain marginal likelihood. If shape B is used

instead, the EDM mapping causes a larger mismatch between the mapped measurement-induced extension $V_{f,k}^{i,(B)}$ and the predicted extension $V_{f,k|k-1}^{i,(B)}$, leading to a smaller marginal likelihood. Therefore, a shape hypothesis that better matches the true contour produces a smaller EDM-domain extension discrepancy and a larger marginal likelihood. In this way, shape information enters the PMBM association process through the EDM-domain likelihood, rather than through an additional shape decision rule.

4.2. Extend Difference Mapping

This section gives the construction of the EDM scaling function. For association likelihood evaluation at scan k, the predicted irregular contour $\hat{C}_{c,k|k-1}$ and the predicted ellipsoidal baseline $\hat{C}_{e,k|k-1}$ are represented by radial functions in the same polar coordinate frame. Their direction-dependent radial ratio defines the predicted EDM mapping used for candidate measurement subsets.

Considering that the construction of the EDM must be consistent with the random-matrix model and maintain low computational complexity, the baseline ellipsoidal contour used for current association is obtained from the predicted extension state $X_{k|k-1}^{j,i}$ of the corresponding Bernoulli component. After association is selected, the assigned measurement subset is used to update the posterior extension state and the posterior baseline ellipsoidal contour. Let $V_{e,k}$ denote the positive definite matrix parameter corresponding to this ellipsoidal representation; then the radial function of this baseline ellipsoidal contour in direction θ_n can be written as

$$\rho_{e,k}(\theta_n) = \sqrt{\begin{bmatrix}\cos\theta_n \\ \sin\theta_n\end{bmatrix}^{\mathrm{T}} V_{e,k} \begin{bmatrix}\cos\theta_n \\ \sin\theta_n\end{bmatrix}}, n = 1, 2, \ldots, N, \tag{50}$$

where $\rho_{e,k}(\theta_n)$ denotes the radial sample of the baseline ellipsoidal contour in direction θ_n. By computing for all sector center directions $\{\theta_n\}_{n=1}^{N}$, one obtains the set of radial samples of the ellipsoidal baseline at discrete angles

$$\left\{\rho_{e,k}(\theta_n)\right\}_{n=1}^{N}. \tag{51}$$

Since the irregular contour parameter $\hat{C}_{c,k}$ has already been parameterized in the form of a Fourier series, to ensure that the two types of contours share a unified representation for the subsequent EDM construction, the baseline ellipsoidal contour $\hat{C}_{e,k}$ is also expressed as a Fourier series of the same order. Its parametric representation is denoted as

$$\hat{C}_{e,k} = \left(\widetilde{a}_{0,k}, \{\widetilde{a}_{j,k}\}_{j=1}^{J}, \{\widetilde{b}_{j,k}\}_{j=1}^{J}\right), \tag{52}$$

where $\hat{a}_{0,k}$ is the zero-order Fourier coefficient of the ellipsoidal baseline, $\hat{a}_{j,k}$ and $\hat{b}_{j,k}$ are the cosine and sine Fourier coefficients of order j, respectively, and J is the maximum Fourier order.

The radial function of the ellipsoidal baseline can be written, with reference to Equation (26), as

$$\mathcal{F}(\hat{C}_{e,k};\theta) = \frac{\widetilde{a}_{0,k}}{2} + \sum_{j=1}^{J}\left(\widetilde{a}_{j,k}\cos(j\theta) + \widetilde{b}_{j,k}\sin(j\theta)\right), \tag{53}$$

$$\widetilde{a}_{0,k} = \frac{1}{N}\sum_{n=1}^{N}\rho_{e,k}(\theta_n), \tag{54}$$

$$\widetilde{a}_{j,k} = \frac{2}{N}\sum_{n=1}^{N}\rho_{e,k}(\theta_n)\cos(j\theta_n), j = 1,2,\ldots,J, \tag{55}$$

$$\widetilde{b}_{j,k} = \frac{2}{N}\sum_{n=1}^{N}\rho_{e,k}(\theta_n)\sin(j\theta_n), j = 1,2,\ldots,J, \tag{56}$$

where the Fourier coefficients $\widetilde{a}_{0,k}$, $\widetilde{a}_{j,k}$, and $\widetilde{b}_{j,k}$ are obtained from the discrete radial samples $\{\rho_{e,k}(\theta_n)\}_{n=1}^{N}$ via the discrete Fourier relations.

After the parametric representation of the baseline ellipsoidal contour is obtained from (54), the irregular contour parameter $\hat{C}_{c,k}$ and the ellipsoidal baseline parameter $\hat{C}_{e,k}$ take a consistent functional form, so that their radial differences can be directly compared in each direction, and the EDM scaling function can be further constructed.

Let $\mathcal{F}(\hat{C}_{c,k};\theta)$ and $\mathcal{F}(\hat{C}_{e,k};\theta)$ denote the radial functions of the irregular contour estimate and the ellipsoidal baseline in the same direction, respectively, as

$$f_{\mathrm{EDM},k}(\theta) = \frac{\mathcal{F}(\hat{C}_{c,k};\theta)}{\mathcal{F}(\hat{C}_{e,k};\theta)}, \theta \in [0,2\pi), \tag{57}$$

For the discrete angular partition, the raw EDM ratio in the n-th direction is computed as

$$\psi^{*}_{k,n} = \frac{\mathcal{F}(\hat{C}_{c,k};\theta_n)}{\mathcal{F}(\hat{C}_{e,k};\theta)}, n = 1,2,\ldots,N. \tag{58}$$

Since both $\hat{C}_{c,k}$ and $\hat{C}_{e,k}$ are derived from noisy finite measurements, the bounded instantaneous ratio $\psi_{k,n}$ may still fluctuate over time. If it is directly used to map the original measurement set, the mapping result will be sensitive to contour estimation errors, thus affecting the robustness of the EDM-domain extension state estimation. For this reason, Kalman recursive smoothing is applied to the ratio sequence in each direction separately.

Let $\psi^{*}_{k,n}$ denote the true but unknown EDM ratio state in the n-th direction, and adopt a random walk model to describe its temporal variation:

$$\psi^{*}_{k,n} = \psi^{*}_{k-1,n} + w_{k,n}, \tag{59}$$

where $w_{k,n}$ is zero-mean process noise with variance Q_n. After association has been determined, the discrete ratio computed from the assigned measurement subset is treated as a noisy observation of the EDM ratio state,

$$\psi_{k,n} = \psi^{*}_{k,n} + \eta_{k,n}, \tag{60}$$

where $\eta_{k,n}$ is zero-mean observation noise with variance R_n.

Denote $\hat{\psi}_{k|k-1,n}$ and $\hat{\psi}_{k|k,n}$ as the predicted and posterior estimates of the EDM ratio in the n-th direction, respectively, and let $P_{k|k-1,n}$ and $P_{k|k,n}$ be the corresponding error variances. The Kalman prediction step is

$$\hat{\psi}_{k|k-1,n} = \hat{\psi}_{k-1|k-1,n}, \tag{61}$$

$$P_{k|k-1,n} = P_{k-1|k-1,n} + Q_n, \tag{62}$$

and the Kalman gain is

$$\mathcal{K}_{k,n} = \frac{P_{k|k-1,n}}{P_{k|k-1,n} + R_n}. \tag{63}$$

The update step can then be written as

$$\hat{\psi}_{k|k,n} = \hat{\psi}_{k|k-1,n} + \mathcal{K}_{k,n}\left(\psi_{k,n} - \hat{\psi}_{k|k-1,n}\right), \tag{64}$$

$$P_{k|k,n} = (1 - \mathcal{K}_{k,n})P_{k|k-1,n}. \tag{65}$$

For likelihood evaluation at the current scan, the EDM ratio used for measurement mapping is the predicted smoothed ratio propagated from the previous posterior. Since the angular direction of a measurement point usually does not exactly coincide with a sector center direction, piecewise linear interpolation of the predicted ratio values from two adjacent directions is used to obtain a continuous predicted EDM function over the angular interval. The posterior smoothed ratio updated from the assigned measurement subset is stored and used only from the subsequent scan.

For a candidate measurement subset Z_k^h and the i-th Bernoulli component under the j-th global hypothesis, the angle of a measurement point $z \in Z_k^h$ with respect to the predicted target center is defined as

$$\theta(z) = \text{atan2}\left(z_y - m^{j,i}_{k|k-1,y}, z_x - m^{j,i}_{k|k-1,x}\right). \tag{66}$$

The mapped point in the EDM domain is obtained using the predicted EDM function:

$$z_f = m^{j,i}_{k|k-1} + f^{j,i}_{\text{EDM},k|k-1}(\theta(z))\left(z - m^{j,i}_{k|k-1}\right), z \in Z_k^C. \tag{67}$$

Thus, the mapped candidate subset is

$$Z_{f,k}^{h,(j,i)} = Map\left(Z_k^h, f^{j,i}_{\text{EDM},k|k-1}\right). \tag{68}$$

In these equations, Z_k^h denotes a candidate measurement subset at scan k, $m^{j,i}_{k|k-1}$ denotes the predicted center of the i-th Bernoulli component under the j-th global hypothesis, z_f denotes the mapped measurement point in the EDM domain, and $Z_{f,k}^{h,(j,i)}$ denotes the EDM-domain measurement subset obtained under the predicted EDM function of that local hypothesis.

Equations (66)–(68) indicate that the EDM mapping keeps the angular information of each measurement point relative to the target center unchanged, and only adjusts its radial position with a direction-dependent scaling. After this mapping transformation, the candidate measurement subset is represented in the EDM domain under the predicted shape information carried by the corresponding Bernoulli hypothesis. This mapped subset is used only for likelihood evaluation before association. The posterior EDM function updated from the assigned subset is not used in this likelihood evaluation.

The EDM mapping is centered at the predicted target center of the corresponding Bernoulli hypothesis. The same center and coordinate frame are used for both the irregular contour and the ellipsoidal baseline. To reduce the influence of temporary estimation errors, the EDM ratio is recursively smoothed and constrained within a positive bounded interval. If the assigned subset is sparse or the kinematic innovation is abnormal, the posterior shape update is weakened or skipped.

4.3. Extended Difference Mapping and Its PMBM Filter Recursion

Before introducing the EDM-GGIW recursion, the temporal order of the proposed filter should be clarified. The contour parameter, ellipsoidal baseline, and EDM radial ratio used for current association are obtained from the prior prediction propagated from the previous posterior. The current measurement subset is not first used to construct a posterior contour and then reused to evaluate its own likelihood. Instead, it enters the recursion only as a candidate measurement cell to be evaluated by the predicted EDM-domain likelihood.

After a target-cell association is selected, the associated measurement subset is then used to update the contour parameter and EDM ratio. The updated shape information is stored as posterior information and used for the next prediction step.

To facilitate the introduction of EDM into the target extension state recursion, the EDM-GGIW component parameter for a target at time k is defined as

$$\zeta_{\mathrm{EDM},k} = \left\{ \alpha_{f,k}, \beta_{f,k}, m_{f,k}, P_{f,k}, \nu_{f,k}, V_{f,k}, V_k, \hat{C}_{c,k}, \hat{C}_{e,k} \right\}, \tag{69}$$

where $\gamma_{f,k} = \left\{ \alpha_{f,k}, \beta_{f,k} \right\}$ is the measurement rate parameter in the EDM domain, following a Gamma distribution; $\xi_{f,k} = \{ m_{f,k}, P_{f,k} \}$ is the kinematic state parameter in the EDM domain, following a Gaussian distribution; $X_{f,k} = \{ \nu_{f,k}, V_{f,k}, V_k \}$ is the extension shape parameter in the EDM domain, corresponding to an inverse-Wishart distribution, and V_k denotes the scale matrix parameter of the baseline ellipsoid in the original measurement domain; $\hat{C}_{c,k}$ and $\hat{C}_{e,k}$ represent the irregular contour estimate parameter and the ellipsoidal baseline estimate parameter, respectively.

Thus, the single-target state $x_{f,k}$ in the EDM domain and its GGIW density $p_{\mathrm{EDM}}(x_{f,k}; \zeta_{\mathrm{EDM},k})$ are given by

$$x_{f,k} = \left\{ \gamma_{f,k}; \xi_{f,k}; X_{f,k} \right\}, \tag{70}$$

$$p_{\mathrm{EDM}}\left(x_{f,k}; \zeta_{\mathrm{EDM},k} \right) = \mathcal{G}\left(\gamma_k; \alpha_{f,k}, \beta_{f,k} \right) \mathcal{N}\left(\xi_k; m_{f,k}, P_{f,k} \right) \mathcal{IW}\left(X_{f,k}; \nu_{f,k}, V_{f,k} \right). \tag{71}$$

4.3.1. The Shape Hypothesis in PMBM

The maintenance and pruning of candidate shape hypotheses follow the PMBM hypothesis management. A candidate shape hypothesis $h_k^{j,i}$ is attached to a local target hypothesis rather than maintained as an independent shape template. When a new Bernoulli component is initialized by a measurement subset, its initial contour parameter $\hat{C}_{c,k}^{j,i}$ is reconstructed by angular partitioning and Fourier series estimation, and its initial ellipsoidal baseline $\hat{C}_{e,k}^{j,i}$ is obtained from the corresponding ellipsoidal extension estimate. The initial EDM scaling function $f_{\mathrm{EDM},k}^{j,i}(\theta)$ is then constructed from the ratio between these two contours.

When an existing local target hypothesis is associated with a non-empty measurement subset, its candidate shape hypothesis is updated by the EDM-GGIW update and the shape estimation step. The assigned measurement subset updates the irregular contour, the ellipsoidal baseline, and the EDM radial scaling function. When missed detection occurs, no new contour is reconstructed from measurements, and the candidate shape hypothesis is predicted or retained from the previous time step.

Therefore, candidate shape hypotheses are instantiated, maintained, and pruned together with the PMBM local and global hypotheses. If a local target hypothesis or a global hypothesis is removed during PMBM pruning, merging, or global hypothesis selection, its attached candidate shape hypothesis is removed at the same time. No additional shape-template enumeration or shape-template pruning is introduced.

4.3.2. EDM Transformation Density and PMBM Likelihood

To incorporate EDM mapping into the PMBM likelihood, the density change induced by the radial transformation is considered. For a candidate measurement subset Z_C associated with the i-th Bernoulli component under global hypothesis j, the EDM function used for likelihood evaluation is the predicted function $f_{\mathrm{EDM},k|k-1}^{j,i}(\theta)$. For a single measurement $z \in Z_C$, the mapped point in the EDM domain is

$$z_f = m_k + f_{\mathrm{EDM},k|k-1}^{j,i}(\theta(z))(z - m_k), \tag{72}$$

where m_k is the predicted or filtered target center, and $\theta(z)$ is the angle of $z - m_k$. In polar coordinates with respect to m_k, the mapping can be written as

$$r_f = f^{j,i}_{\mathrm{EDM},k|k-1}(\theta) r, \theta_f = \theta. \tag{73}$$

Therefore, the two-dimensional Jacobian determinant of the EDM mapping is

$$\left| J^{j,i}_{\mathrm{EDM},k}(z) \right| = \left[f^{j,i}_{\mathrm{EDM},k|k-1}(\theta(z)) \right]^2. \tag{74}$$

Let

$$Z_{f,k} = \mathrm{Map}\left(Z_C, f^{j,i}_{\mathrm{EDM},k|k-1} \right) \tag{75}$$

denote the mapped measurement subset in the EDM domain. If $\ell_f(Z_{f,k} \mid x_f)$ is the standard extended-target likelihood evaluated in the EDM domain, then the corresponding EDM-induced likelihood in the original measurement domain is

$$\ell_{\mathrm{EDM}}(Z_C \mid x_f) = \left[\prod_{z \in Z_C} \left| J^{j,i}_{\mathrm{EDM},k}(z) \right| \right] \ell_f(Z_{f,k} \mid x_f). \tag{76}$$

After marginalizing the predicted EDM-GGIW density, the single-target marginal likelihood used in the PMBM association weight becomes

$$\ell^{j,i}_{\mathrm{EDM}}(Z_C) = \left[\prod_{z \in Z_C} | J^{j,i}_{\mathrm{EDM},k}(z) | \right] \int \ell_f(Z_{f,k} \mid x_f) p_{\mathrm{EDM}}\left(x_f; \zeta^{j,i}_{\mathrm{EDM},k|k-1} \right) dx_f. \tag{77}$$

This equation shows that the transformed measurements are not treated as ordinary GGIW measurements without correction. The GGIW likelihood is evaluated in the EDM domain, while the Jacobian product accounts for the probability-volume change caused by the radial transformation. Since $f^{j,i}_{\mathrm{EDM},k|k-1}(\theta)$ depends on the predicted shape state carried by the local Bernoulli component, the Jacobian term is generally not a common constant among different local association hypotheses.

For the PMBM update, the recursive structure remains unchanged. The ordinary single-target marginal likelihood is replaced by the EDM-induced marginal likelihood $\ell^{j,i}_{\mathrm{EDM}}(Z_C)$. Thus, EDM enters the PMBM update through the transformed single-target likelihood, while the PMBM hypothesis management, missed-detection term, clutter normalization, and global hypothesis normalization are retained.

It should be noted that the exact transformed noise covariance may become direction-dependent after the nonlinear radial mapping. To preserve the closed-form GGIW recursion, the mapped measurement set $Z_{f,k}$ is modeled by the GGIW likelihood in the EDM domain as an approximation, while the Jacobian term explicitly corrects the probability-volume change in the transformation.

4.4. EDM-GGIW State Update and Prediction

4.4.1. EDM Update

Let Z^C_k be the measurement subset assigned to a Bernoulli component after association evaluation. The association likelihood of this subset has already been computed using the predicted EDM function $f^{j,i}_{\mathrm{EDM},k|k-1}(\theta)$, as described in Section 4.3.2. In the posterior update below, the same mapped subset obtained under the predicted EDM function is used to update the EDM-GGIW state $Z^{C,(j,i)}_{f,k} = Map\left(Z^C_k, f^{j,i}_{\mathrm{EDM},k|k-1} \right)$:

For convenience, the EDM-domain sample covariance matrix is denoted as

$$\Sigma_{f,k}^{C,(j,i)} = \sum_{z \in Z_{f,k}^{C,(j,i)}} (z - \bar{z}_{f,k}^{C,(j,i)})(z - \bar{z}_{f,k}^{C,(j,i)})^T, \tag{78}$$

$$\bar{z}_{f,k}^{C,(j,i)} = \frac{1}{\left|Z_{f,k}^{C,(j,i)}\right|} \sum_{z \in Z_{f,k}^{C,(j,i)}} z. \tag{79}$$

Correspondingly, the sample covariance matrix of the assigned original-domain subset is

$$\Sigma_k^C = \sum_{z \in Z_k^C} (z - \bar{z}_k^C)(z - \bar{z}_k^C)^T, \tag{80}$$

$$\bar{z}_k^C = \frac{1}{|Z_k^C|} \sum_{z \in Z_k^C} z. \tag{81}$$

Here, Z_k^C denotes the assigned measurement subset in the original domain, $Z_{f,k}^{C,(j,i)}$ denotes its mapped version in the EDM domain under the predicted EDM function, $\Sigma_{f,k}^{C,(j,i)}$ denotes the EDM-domain scatter matrix, and Σ_k^C denotes the original-domain scatter matrix. The posterior EDM function $f_{\mathrm{EDM},k}^{j,i}(\theta)$ is updated only after this posterior state update and is stored for the next scan.

The update of the measurement rate parameter $\gamma_{f,k} = \{\alpha_{f,k}, \beta_{f,k}\}$ is

$$\gamma_{f,k} = \begin{cases} \alpha_{f,k} = \alpha_{f,k|k-1} + \mid Z_{f,k} \mid, \\ \beta_{f,k} = \beta_{f,k|k-1} + 1 \end{cases} \tag{82}$$

The update of the kinematic state $\xi_{f,k} = \{m_{f,k}, P_{f,k}\}$ is

$$\xi_{f,k} = \begin{cases} m_{f,k} == m_{f,k|k-1} + K_{f,k}\varepsilon_{f,k} \\ P_{f,k} == P_{f,k|k-1} - K_{f,k}S_{f,k}K_{f,k}^{\mathrm{T}} \end{cases}, \tag{83}$$

$$X_{f,k|k-1} = \bar{X}_{f,k|k-1} + R_k, \tag{84}$$

$$K_{f,k} = P_{f,k|k-1}H^{\mathrm{T}}S_{f,k}^{-1}, \tag{85}$$

$$S_{f,k} = HP_{f,k|k-1}H^{\mathrm{T}} + \frac{X_{f,k|k-1}}{\mid Z_{f,k} \mid}. \tag{86}$$

The update of the extension shape parameter $X_{f,k} = \left\{\nu_{f,k}, V_{f,k}, V_k\right\}$ is

$$X_{f,k} = \begin{Bmatrix} V_{f,k} & = V_{f,k|k-1} + N_{f,k} + \Sigma_{f,k}, \\ \nu_{f,k} & = \nu_{f,k|k-1} + \mid Z_{f,k} \mid, \\ V_k & = V_{k|k-1} + N_k + \Sigma_k \end{Bmatrix}, \tag{87}$$

$$N_{f,k} = \bar{X}_{f,k|k-1}^{1/2} S_{f,k}^{-1/2} \varepsilon_{f,k} \varepsilon_{f,k}^{\mathrm{T}} S_{f,k}^{-\mathrm{T}/2} \bar{X}_{f,k|k-1}^{\mathrm{T}/2}, \tag{88}$$

$$N_k = \bar{X}_k^{1/2} {S_k}^{-1/2} \varepsilon_f {\varepsilon_f}^{\mathrm{T}} {S_k}^{-\mathrm{T}/2} \bar{X}_k^{\mathrm{T}/2}, \tag{89}$$

$$\varepsilon_{f,k} = \bar{z}_{f,k} - Hm_{f,k|k-1}. \tag{90}$$

Propagating in the EDM domain also requires updating the ellipsoidal baseline parameter $\hat{C}_{e,k}$. Furthermore, after association, the assigned original-domain measurement subset Z_k^C is used to update the posterior baseline ellipsoid parameter V_k. Taking the expectation of V_k in Equation (87),

$$\bar{X}_k = \frac{V_k}{\nu_{f,k} - 2d - 2}, \tag{91}$$

where $\overline{X}_k$ is the posterior mean extension matrix of the original-domain ellipsoidal baseline, and d is the dimension.

Then one can extract the ellipsoidal baseline radial samples in each direction and reconstruct the ellipsoidal modeling parameter $\hat{C}_{e,k}$ according to the discrete Fourier relations in Section 4.2. Meanwhile, the posterior irregular contour parameter is reconstructed following Section 4.3, using the angular partition results and local extension components of the assigned original-domain measurement subset Z_k^C.

Thus, the state update likelihood in the EDM domain is obtained as

$$\ell_{\mathrm{EDM}} = \left(\pi^{|Z_{f,k}|} \mid Z_{f,k} \mid\right)^{-d/2} \frac{\mid V_{f,k|k-1} \mid^{\mathbb{v}(\nu_{f,k|k-1})} \Gamma_d(\nu_{f,k}) \mid X_{f,k} \mid^{1/2} \mathbb{G}(\alpha_{f,k}, \beta_{f,k|k-1})}{\mid V_{f,k} \mid^{\mathbb{v}(\nu_{f,k})} \Gamma_d(\nu_{f,k|k-1}) \mid S_{f,k} \mid^{1/2} \mathbb{G}(\alpha_{f,k|k-1}, \beta_{f,k})}, \quad (92)$$

where

$$\mathbb{v}(\nu) = \frac{\nu - d - 1}{2}, \quad (93)$$

$$\mathbb{G}(\alpha, \beta) = \Gamma(\alpha)(\beta)^{\alpha}. \quad (94)$$

Equation (92) gives the EDM-domain likelihood form used in the posterior update of the assigned subset. Its input is the mapped assigned subset in the EDM domain rather than the untransformed original-domain subset.

4.4.2. EDM Prediction

After the EDM-GGIW update at time k, the prediction for the next time step follows the recursive form of the GGIW. For the EDM-domain measurement rate parameters,

$$\gamma_{f,k+1|k} = \begin{cases} \alpha_{f,k+1|k} = \frac{\alpha_{f,k}}{\eta} \\ \beta_{f,k+1|k} = \frac{\beta_{f,k}}{\eta} \end{cases}, \quad (95)$$

For the kinematic state,

$$\xi_{f,k+1|k} = \begin{cases} m_{f,k+1|k} = F_k(m_{f,k}) \\ P_{f,k+1|k} = G_k P_{f,k} G_k^{\mathrm{T}} + Q_k \end{cases}, \quad (96)$$

For the extension shape,

$$X_{f,k+1|k} = \begin{cases} \nu_{f,k+1|k} = \nu_{f,k} + e^{-T_s/\tau}(\nu_{f,k} - 2d - 2) \\ V_{f,k+1|k} = e^{-T_s/\tau} M(\xi_k) V_{f,k} M(\xi_k)^{\mathrm{T}} \\ V_{k+1|k} = e^{-T_s/\tau} M(\xi_k) V_k M(\xi_k)^{\mathrm{T}} \end{cases}, \quad (97)$$

In Equations (95)–(97), η is the measurement rate parameter; G is a transformation matrix with $G = \nabla_{\xi} F(m)$; m is the target kinematic state; P is the error covariance matrix; R is the process noise covariance; d is the scene dimension; τ is the maneuver correlation constant; T_s is the sampling period; $F(\cdot)$ is the kinematic state transition matrix; and $M(\cdot)$ is the state transformation matrix.

Taking the expectation of $V_{k+1|k}$ in Equation (97) yields

$$V_{e,k} = \frac{V_{k+1|k}}{\nu_{f,k+1|k} - 2d - 2}, \quad (98)$$

from which the discrete radial samples of the ellipsoidal baseline at the predicted time step can be obtained. These samples are then used to fit the predicted contour parameter $\hat{C}_{e,k+1|k}$ via the discrete Fourier relations described in Section 4.2. As for the shape contour parameter $\hat{C}_{c,k}$,

$$\hat{C}_{c,k+1|k} = \hat{C}_{c,k}. \quad (99)$$

This is feasible because $\hat{C}_{c,k}$ is not part of the random-matrix state but rather the irregular contour parameter reconstructed from measurements. In the prediction stage, maintaining its parameters to be unchanged is a simple and stable approach in the absence of extra shape evolution priors. If a relevant shape evolution model is available, the corresponding parameters can be added accordingly.

Based on the single-target GGIW component prediction and update process in the EDM domain, the EDM-related single-target likelihood and state recursion results can be further embedded into the PMBM multi-target filter. The complete implementation of the EDM-PMBM filter is described in Tables 5 and 6.

Table 5. EDM domain prediction pseudocode.

1.	**Input:** posterior EDM-GGIW parameter $\zeta^{j,i}_{\mathrm{EDM},k}$, posterior irregular contour $\hat{C}^{j,i}_{c,k}$, posterior ellipsoidal baseline $\hat{C}^{j,i}_{e,k}$, posterior discrete EDM ratio $\hat{\psi}^{j,i}_{k|k,n}$, posterior ratio covariance $\mathcal{P}^{j,i}_{k|k,n}$, and the dynamic model parameters at scan k.
2.	**Output:** predicted EDM-GGIW parameter $\zeta^{j,i}_{\mathrm{EDM},k+1|k}$, predicted irregular contour $\hat{C}^{j,i}_{c,k+1|k}$, predicted ellipsoidal baseline $\hat{C}^{j,i}_{e,k+1|k}$, predicted discrete EDM ratio $\hat{\psi}^{j,i}_{k+1|k,n}$, predicted ratio covariance $\mathcal{P}^{j,i}_{k+1|k,n}$, and predicted EDM function $f^{j,i}_{\mathrm{EDM},k+1|k}(\theta)$.
3.	Predict the EDM-domain measurement rate parameter $\gamma^{j,i}_{f,k+1|k} = \{\alpha^{j,i}_{f,k+1|k}, \beta^{j,i}_{f,k+1|k}\}$, refer to Equation (95).
4.	Predict the EDM-domain kinematic parameter $\xi^{j,i}_{f,k+1|k} = \{m^{j,i}_{f,k+1|k}, P^{j,i}_{f,k+1|k}\}$, refer to Equation (96).
5.	Predict the EDM-domain extension parameter $X^{j,i}_{f,k+1|k} = \{\nu^{j,i}_{f,k+1|k}, V^{j,i}_{f,k+1|k}\}$, refer to the GGIW extension prediction equation. Here, $\nu^{j,i}_{f,k+1|k}$ is the predicted inverse-Wishart degrees-of-freedom parameter and $V^{j,i}_{f,k+1|k}$ is the predicted inverse-Wishart scale matrix. If the current manuscript numbering is retained, refer to the corresponding extension prediction equation used around Equation (97).
6.	Predict the original-domain extension parameter $V^{j,i}_{k+1|k}$, refer to Equation (97).
7.	Compute the predicted mean extension matrix of the original-domain ellipsoidal baseline : $\bar{X}^{j,i}_{e,k+1|k} = \frac{V^{j,i}_{k+1|k}}{\nu^{j,i}_{f,k+1|k}-2d-2}$, refer to Equation (98).
8.	Extract the predicted ellipsoidal radial samples $\left\{\rho^{j,i}_{e,k+1|k}(\theta_n)\right\}_{n=1}^{N}$ from $\bar{X}^{j,i}_{e,k+1|k}$, refer to Equation (50)–(52). Then reconstruct the predicted ellipsoidal baseline parameter $\hat{C}^{j,i}_{e,k+1|k}$ using the discrete Fourier relations, refer to Equations (53)–(56).
9.	Propagate the irregular contour parameter : $\hat{C}^{j,i}_{c,k+1|k}$, refer to Equation (99).
10.	For each angular direction $n = 1, \ldots, N$, predict the discrete EDM ratio state: $\hat{\psi}^{j,i}_{k+1|k,n}$, refer to Equation (61). Here, $\hat{\psi}^{j,i}_{k|k,n}$ is the posterior EDM ratio at scan k, and $\hat{\psi}^{j,i}_{k+1|k,n}$ is its predicted value for scan $k+1$.
11.	Predict the ratio covariance : $\mathcal{P}^{j,i}_{k+1|k,n}$, refer to Equation (62).
12.	Interpolate the predicted discrete ratio sequence $\left\{\hat{\psi}^{j,i}_{k+1|k,n}\right\}_{n=1}^{N}$ over $\theta \in [0,\ 2\pi)$ to obtain the predicted continuous EDM function $f^{j,i}_{\mathrm{EDM},k+1|k}(\theta)$, following the interpolation operation after Equation (65).
13.	Assemble the predicted EDM-GGIW parameter : $\zeta^{j,i}_{\mathrm{EDM},k+1|k}$

Table 6. EDM domain update pseudocode.

1.	**Input:** Candidate measurement subset Z^C_k, predicted EDM-GGIW parameter $\zeta^{j,i}_{\mathrm{EDM},k|k-1}$, predicted irregular contour $\hat{C}^{j,i}_{c,k|k-1}$, predicted ellipsoidal baseline $\hat{C}^{j,i}_{e,k|k-1}$, predicted discrete EDM ratio $\hat{\psi}^{j,i}_{k|k-1,n}$, predicted ratio covariance $\mathcal{P}^{j,i}_{k|k-1,n}$, and predicted EDM function $f^{j,i}_{\mathrm{EDM},k|k-1}(\theta)$. Here, Z^C_k denotes a candidate measurement subset at scan k, rather than the entire measurement set.
2.	**Output:** EDM-induced association likelihood $\phi^{j,i}_{\mathrm{EDM}}(Z^C_k)$. If the association is selected, output the posterior EDM-GGIW parameter $\zeta^{j,i}_{\mathrm{EDM},k}$, posterior irregular contour $\hat{C}^{j,i}_{c,k}$, posterior ellipsoidal baseline $\hat{C}^{j,i}_{e,k}$, posterior discrete EDM ratio $\hat{\psi}^{j,i}_{k|k,n}$, posterior ratio covariance $\mathcal{P}^{j,i}_{k|k,n}$, and posterior EDM function $f^{j,i}_{\mathrm{EDM},k}(\theta)$.

Table 6. *Cont.*

3.	**Stage I: Prior EDM likelihood evaluation for association. This stage uses only predicted EDM information. No posterior contour, EDM ratio, or EDM function is updated in this stage.**
4.	Use the predicted EDM function $f^{j,i}_{\mathrm{EDM},k\|k-1}(\theta)$ carried by the local Bernoulli hypothesis. This function is obtained from the predicted discrete EDM ratio sequence $\left\{\hat{\psi}^{j,i}_{k\|k-1,n}\right\}_{n=1}^{N}$, following the interpolation operation after Equation (65).
5.	For each measurement point $z \in Z_k^C$, compute its angle with respect to the predicted target center $m^{j,i}_{k\|k-1}$ according to Equation (66). Here, $m^{j,i}_{k\|k-1}$ is the predicted target center of the i-th Bernoulli component under the j-th global hypothesis.
6.	Map the candidate measurement subset into the EDM domain using the predicted EDM function, refer to Equations (66)–(68) after replacing $f_{\mathrm{EDM},k}$ with $f^{j,i}_{\mathrm{EDM},k\|k-1}$: $z_f = m^{j,i}_{k\|k-1} + f^{j,i}_{\mathrm{EDM},k\|k-1}(\theta(z))(z - m^{j,i}_{k\|k-1}), z \in Z_k^C, Z^{C,(j,i)}_{f,k} = Map(Z_k^C, f^{j,i}_{\mathrm{EDM},k\|k-1})$. Here, $Z^{C,(j,i)}_{f,k}$ is the EDM-domain mapped subset under the predicted EDM function of the local hypothesis (j,i).
7.	Compute the Jacobian determinant of the predicted EDM mapping for each $z \in Z_k^C$, and form the Jacobian product according to Equation (74)
8.	Evaluate the standard extended-target likelihood $\ell_f\left(Z^{C,(j,i)}_{f,k}\|x_f\right)$ in the EDM domain. Here, x_f denotes the EDM-domain single-target state.
9.	Marginalize the predicted EDM-GGIW density to obtain the EDM-induced association likelihood, according to Equation (77)
10.	Use $\ell^{j,i}_{\mathrm{EDM}}(Z_k^C)$ only for PMBM local hypothesis weighting and global association selection.
11.	Do not update $\hat{C}^{j,i}_{c,k}$, $\hat{C}^{j,i}_{e,k}$, $\hat{\psi}^{j,i}_{k\|k,n}$, $\mathcal{P}^{j,i}_{k\|k,n}$, or $f^{j,i}_{\mathrm{EDM},k}(\theta)$ before the association is selected.
12.	**Stage II: Selected association. If the association between Z_k^C and the Bernoulli component (j,i) is selected, use the mapped subset $Z^{C,(j,i)}_{f,k}$ obtained in Stage I to update the EDM-domain GGIW state. Here, Z_k^C denotes the assigned original-domain measurement subset, and $Z^{C,(j,i)}_{f,k}$ denotes its EDM-domain mapped subset under the predicted EDM function $f^{j,i}_{\mathrm{EDM},k\|k-1}(\theta)$.**
13.	Compute the EDM-domain sample mean and scatter matrix, refer to Equations (78)–(79).
14.	Compute the original-domain sample mean and scatter matrix, refer to Equations (80)–(81)
15.	Update the EDM-domain measurement rate parameter $\gamma^{j,i}_{f,k} = \left\{\alpha^{j,i}_{f,k}, \beta^{j,i}_{f,k}\right\}$, according to Equation (82)
16.	Update the EDM-domain kinematic parameter $\xi^{j,i}_{f,k} = \left\{m^{j,i}_{f,k}, P^{j,i}_{f,k}\right\}$, according to Equation (83)–(86)
17.	Update the EDM-domain and original-domain extension parameters, refer to Equations (87)–(90).
18.	Compute the posterior mean extension matrix of the original-domain ellipsoidal baseline, according to Equation (91)
19.	Interpolate the predicted discrete ratio sequence the posterior ellipsoidal baseline, according to Equations (53)–(56)
20.	Reconstruct the posterior irregular contour after association. Invoke the shape estimator in Table 3 using the assigned original-domain subset Z_k^C, and obtain the posterior irregular contour parameter $\hat{C}^{j,i}_{c,k} = \left(a^{j,i}_{0,k}, \left\{a^{j,i}_{r,k}\right\}_{r=1}^{J}, \left\{b^{j,i}_{r,k}\right\}_{r=1}^{J}\right)$, refer to Equations (38)–(41).
21.	Compute the posterior radial function of the irregular contour $\mathcal{F}(\hat{C}^{j,i}_{c,k};\theta)$, according to Equation (26).
22.	Compute the posterior radial function of the ellipsoidal baseline $\mathcal{F}(\hat{C}^{j,i}_{e,k};\theta)$, according to Equation (53).
23.	Compute the instantaneous posterior EDM ratio in each direction $\psi^{j,i}_{k,n} = \frac{\mathcal{F}(\hat{C}^{j,i}_{c,k};\vartheta_n)}{\mathcal{F}(\hat{C}^{j,i}_{e,k};\vartheta_n)}$, according to Equation (58).
24.	Compute the Kalman gain for the EDM ratio update $\mathcal{K}^{j,i}_{k,n}$, according to Equation (63).
25.	Update the posterior EDM ratio estimate $\hat{\psi}^{j,i}_{k\|k,n}$, according to Equation (64).
26.	Update the posterior ratio covariance $\mathcal{P}^{j,i}_{k\|k,n}$, according to Equation (65).
27.	Construct the posterior EDM function. Interpolate the posterior ratio sequence $\left\{\hat{\psi}^{j,i}_{k\|k,n}\right\}_{n=1}^{N}$ over $\theta \in [0, 2\pi)$ to obtain the posterior EDM function $f^{j,i}_{\mathrm{EDM},k}(\theta) = \mathrm{Interp}\left(\left\{\theta_n \middle\| \hat{\psi}^{j,i}_{k\|k,n}\right\}_{n=1}^{N}\right)$. This operation follows the interpolation description after Equation (65).
28.	Assemble the posterior EDM-GGIW parameter: $\zeta^{j,i}_{\mathrm{EDM},k}$.
29.	Store posterior shape information for the next scan. Store $\hat{C}^{j,i}_{c,k}$, $\hat{C}^{j,i}_{e,k}$, $\hat{\psi}^{j,i}_{k\|k,n}$, $\mathcal{P}^{j,i}_{k\|k,n}$, and $f^{j,i}_{\mathrm{EDM},k}(\theta)$. These posterior quantities are propagated to the next prediction step.
30.	**Special case of initialization: The first detection of a newly generated Bernoulli component is handled by the standard PPP-GGIW birth likelihood. The EDM quantities initialized from the assigned measurement subset are posterior initialization quantities and are used only from the subsequent scan.**

The update in Table 6 is divided into two stages. Stage I performs prior EDM likelihood evaluation for data association. In this stage, each candidate measurement subset Z_k^C is mapped and evaluated using only the predicted EDM function $f^{j,i}_{\mathrm{EDM},k|k-1}(\theta)$ and the predicted EDM-GGIW parameter $\zeta^{j,i}_{\mathrm{EDM},k|k-1}$. No posterior contour or EDM function is updated before association. Stage II is performed only after the association is selected. The assigned measurement subset is then used to update the EDM-GGIW state, reconstruct the posterior contour, update the EDM ratio, and obtain $f^{j,i}_{\mathrm{EDM},k}(\theta)$.

5. Simulation

This section compares the proposed method with GGIW-PMBM, KS-PMBM, BGGIW-PMBM, and GBePMB. To evaluate multi-target tracking performance, the generalized optimal sub-pattern assignment (GOSPA) metric is adopted as the overall error metric. GOSPA simultaneously captures missed detections, false targets, and localization errors. In the experiments, the GOSPA parameters are set as truncation distance $c = 20$ and order $p = 1$.

In addition to GOSPA, this section also introduces an evaluation metric for irregular shape estimation error. Let the radial function corresponding to the true shape C of a target be $\mathcal{F}(C;\theta)$, and let the radial function corresponding to the shape parameter estimate $\hat{C}_c$ obtained by the filter be $\mathcal{F}(\hat{C}_c;\theta)$. The shape error is then defined as

$$\mathrm{ShapeError} = \frac{1}{4\pi^2}\int_0^{2\pi}\left(\mathcal{F}(C;\theta) - \mathcal{F}(\hat{C}_c;\theta)\right)^2 d\theta. \tag{100}$$

It should be noted that the shape error is not incorporated into the overall GOSPA metric; it serves only as an auxiliary indicator to assess the robustness of shape estimation.

This section presents the simulation experimental results. For two different scenarios, 100 Monte Carlo trials are conducted to verify the performance of the proposed EDM-PMBM filter in extended target tracking. In the long-term closely spaced and crossing multi-target scenario, which contains 50 time steps, three targets with different shapes are born simultaneously at the initial time and subsequently undergo close-range parallel and crossing motions. In the complex closely spaced and crossing multi-target scenario, which contains 100 time steps, a total of 10 targets are born at different times and experience multiple complex close-range encounters and crossing processes.

The main parameters of the two simulation scenarios are given in Table 7. To make the new-target initialization process reproducible, Table 7 also lists the PPP-GGIW birth-related parameters used for newly detected Bernoulli components. These parameters include the PPP birth intensity and the GGIW birth parameters for the measurement rate, kinematic state, and ellipsoidal extension. They are used only for the standard PPP-GGIW birth likelihood at the first detection, before any EDM shape information is initialized.

Table 7. Main parameters of the two simulation scenarios.

Parameter	Scenario 1	Scenario 2
Scene size	$S = 400 \times 200$	$S = 700 \times 700$
Dimension	$d = 2$	$d = 2$
Detected probability	$p_D = 0.95$	$p_D = 0.9$
Survival probability	$p_S = 0.99$	$p_S = 0.99$
Poisson rate of target Measurements	$\lambda = 18$	$\lambda = 23$
Poisson rate of clutter	$\lambda_c = 80$	$\lambda_c = 140$
Transformation matrix	$M = \begin{bmatrix} 1 & 0 \\ 0 & 1 \end{bmatrix}$	$M = \begin{bmatrix} 1 & 0 \\ 0 & 1 \end{bmatrix}$
Measurement model	$H = \begin{bmatrix} 1 & 0 & 0 & 0 \\ 0 & 1 & 0 & 0 \end{bmatrix}$	$H = \begin{bmatrix} 1 & 0 & 0 & 0 \\ 0 & 1 & 0 & 0 \end{bmatrix}$

Table 7. *Cont.*

Parameter	Scenario 1	Scenario 2
State transition matrix	$F = \begin{bmatrix} 1 & 1 \\ 0 & 1 \end{bmatrix} \otimes \begin{bmatrix} 1 & 0 \\ 0 & 1 \end{bmatrix}$	$F = \begin{bmatrix} 1 & 1 \\ 0 & 1 \end{bmatrix} \otimes \begin{bmatrix} 1 & 0 \\ 0 & 1 \end{bmatrix}$
Gaussian measurement noise intensity	$R = 0.1$	$R = 0.15$
EDM ratio observation noise variance	R_n =0.01	R_n =0.01
EDM ratio process noise variance	$Q_n = 10^{-4}$	$Q_n = 10^{-4}$
Initial width of each sector	$\mathbb{D}\cdot\sin(\pi/N) = 2.09$	$\mathbb{D}\cdot\sin(\pi/N) = 2.51$
Number of angular partitions for Shape estimation	$N = 36$	$N = 36$
Fourier order	J = 36/2	J = 36/2
Bernoulli pruning threshold	0.01	0.01
PPP pruning threshold	0.01	0.01
PPP Measurements parameter	$\gamma = \{\alpha = 150, \beta = 10\}$	$\gamma = \{\alpha = 120, \beta = 10\}$
PPP Kinematic parameters	$\xi = \{m = [\,], P = [10\ 10\ 20\ 20]\}$	$\xi = \{m = [\,], P = [16\ 16\ 12\ 12]\}$
PPP Extension parameters	$X = \{\nu = 22.5, V = 90.5\}$	$X = \{\nu = 22.5, V = 90.5\}$
Merging threshold	4	4
Weight of global hypothesis (multi-Bernoulli)	0.05	0.05
Weight of the trajectory is still alive	0.0001	0.0001

5.1. Three-Target Long-Term Close Crossing

Scenario 1 evaluates the proposed method in a three-target long-term close-crossing case. The scenario contains 50 time steps, three targets with different non-ellipsoidal shapes, and strong clutter. As shown in Figure 4, the targets enter a close-crossing interval from step 20 to step 45, where measurement partitioning and data association become highly ambiguous.

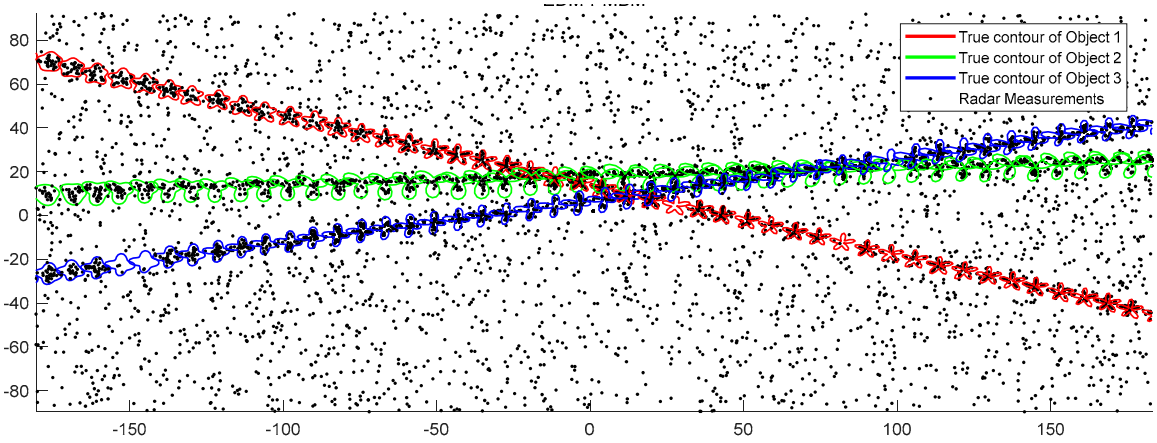


Figure 4. Scenario 2 is the illustration of the multi-target long-term closely spaced and crossing scenario.

Figure 5 shows that the conventional GGIW-PMBM loses one target around step 35 due to component merging. The ellipsoidal model lacks sufficient shape discrimination, leading to confusion and track interruptions.

In contrast, the EDM-PMBM maintains continuous tracking of all three targets throughout (Figure 6). By leveraging contour differences, it effectively distinguishes targets in close crossing, reducing erroneous merging and improving robustness.

Figures 7–10 summarize the quantitative results of Scenario 1. During the close-crossing interval from step 20 to step 45, the compared filters show different degrees of performance degradation. The total GOSPA and missed-detection components indicate that GGIW-PMBM is prone to component merging when the targets are close, while KS-PMBM, BGGIW-PMBM, and GBePMB also suffer from increased association uncertainty. In contrast, EDM-PMBM maintains lower total error and fewer missed detections during the crossing interval.

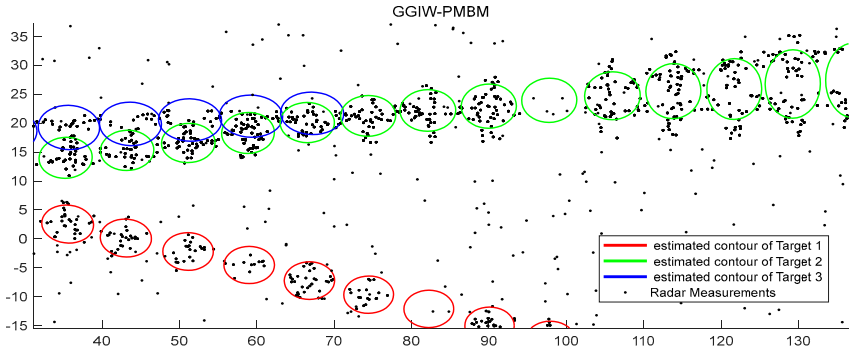


Figure 5. Tracking detail of the GGIW-PMBM.

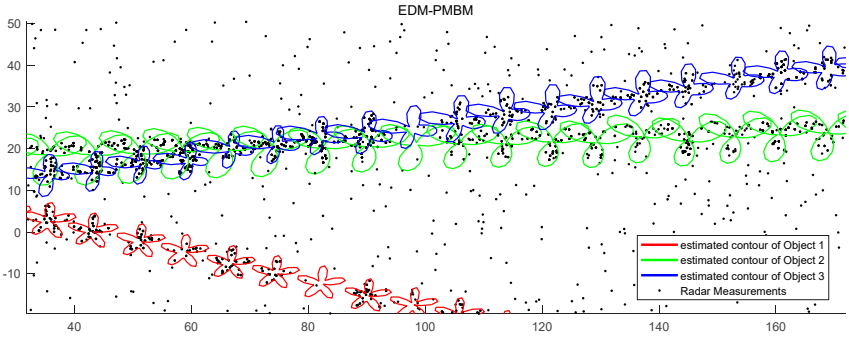


Figure 6. Tracking detail of the EDM-PMBM.

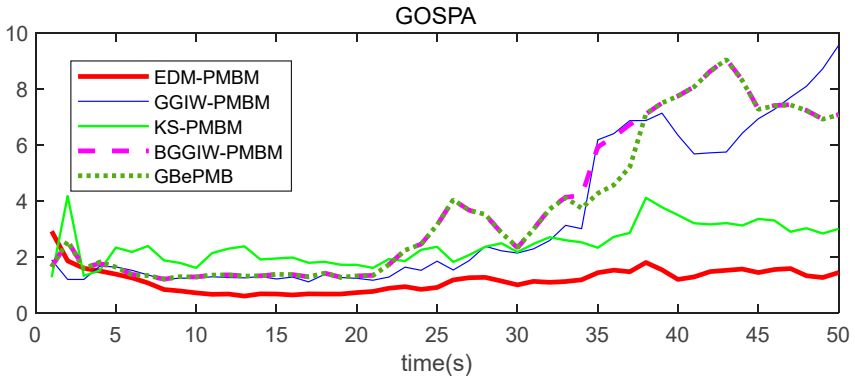


Figure 7. GOSPA error for EDM-PMBM, GGIW-PMBM, KS-PMBM, BGGIW-PMBM, and GBePMB in Scenario 1.

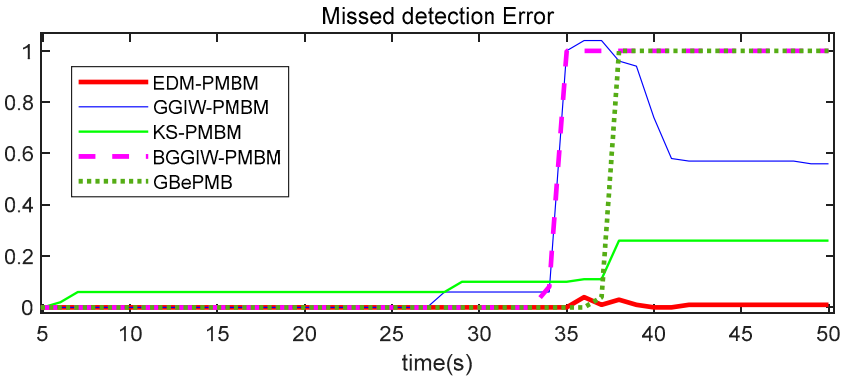


Figure 8. Missed-detection error for the EDM-PMBM, GGIW-PMBM, KS-PMBM, BGGIW-PMBM, and GBePMB filters in Scenario 1.

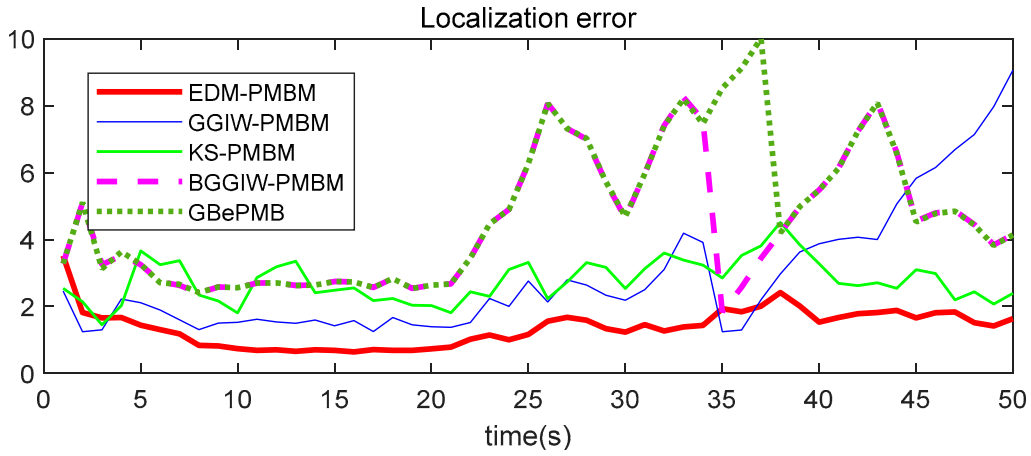


Figure 9. Localization error for the EDM-PMBM, GGIW-PMBM, KS-PMBM, BGGIW-PMBM, and GBePMB filters in Scenario 1.

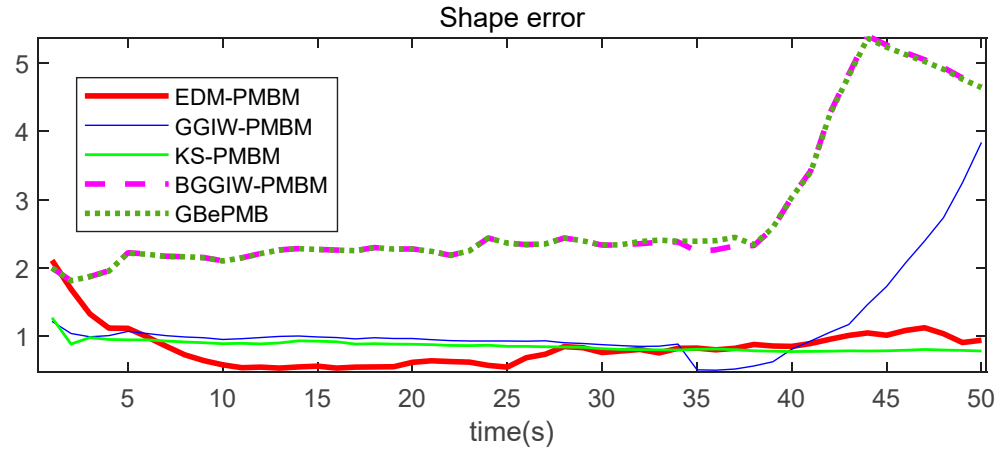


Figure 10. Shape error for the EDM-PMBM, GGIW-PMBM, KS-PMBM, BGGIW-PMBM, and GBePMB filters in Scenario 1.

The localization and shape-error curves further show that EDM-PMBM provides more stable state and contour estimates. The contour-based EDM mapping introduces direction-dependent shape discrimination, which helps separate targets whose ellipsoidal extensions are similar but whose local contour structures differ.

It should be noted that the apparent decrease in localization or shape error for some baseline filters after severe target loss should not be interpreted as a true improvement. Once a target is missed or merged, its localization and shape errors may no longer accumulate in the same way. Therefore, localization and shape-error curves should be interpreted together with the missed-detection component.

Figure 11 reports the time cost of the compared filters in Scenario 1. The result shows that EDM-PMBM has a computational cost close to that of GGIW-PMBM in most time steps. Although EDM-PMBM introduces additional contour reconstruction, EDM mapping, and EDM-domain likelihood evaluation, these operations do not significantly increase the overall runtime under the tested setting. A few time-cost peaks appear during the dense crossing interval, where measurement partitioning and association become more difficult for all filters. Combined with the GOSPA results, EDM-PMBM achieves better tracking accuracy while maintaining a runtime comparable to the standard GGIW-PMBM filter. This indicates that the proposed EDM module improves association discrimination without causing a substantial loss of computational efficiency.

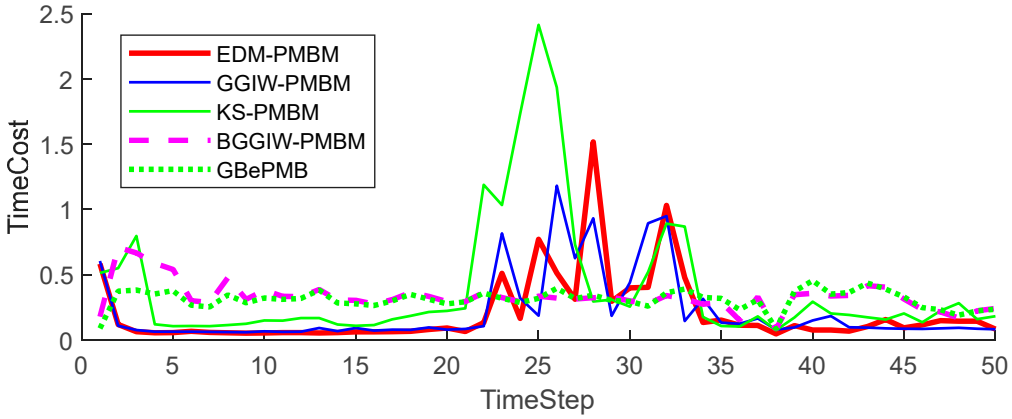


Figure 11. TimeCost for the EDM-PMBM, GGIW-PMBM, KS-PMBM, BGGIW-PMBM, and GBePMB filters in Scenario 1.

5.2. The Multi-Target Complex Closely Spaced and Crossing Scenario

Scenario 2 further evaluates the proposed method in a denser multi-target case. This scenario contains 100 time steps and 10 targets born at different times. The targets undergo repeated aggregation, separation, and crossing events, as shown in Figure 11. Compared with Scenario 1, this setting imposes higher demands on measurement partitioning, data association, and track continuity.

As shown in Figure 12, the scenario features local trajectory crossings as well as simultaneous aggregation, separation, and re-crossing over extended periods, imposing high demands on measurement partitioning, data association, and target discrimination.

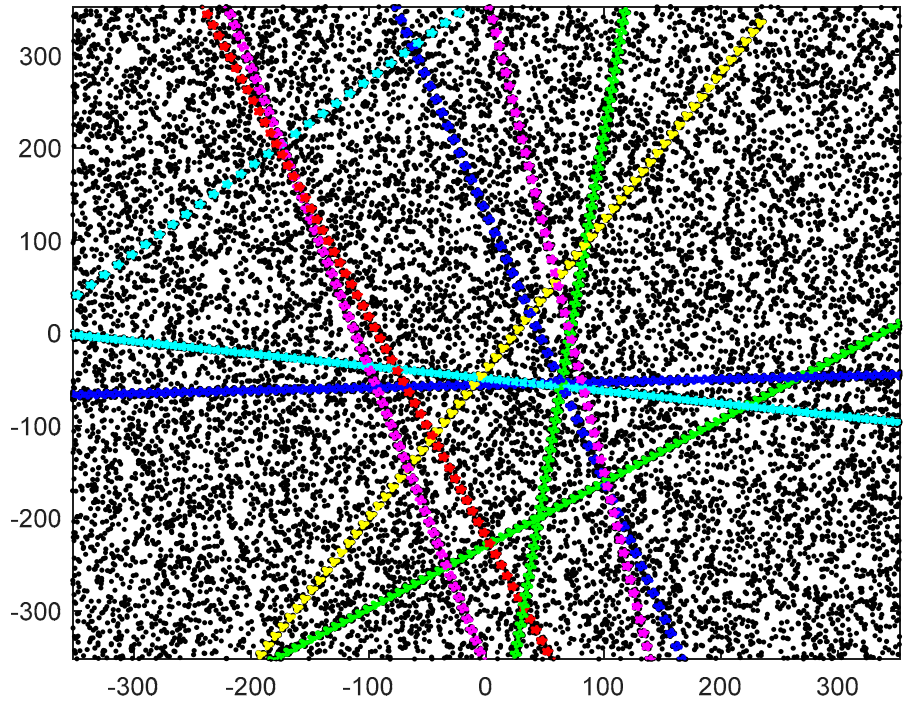


Figure 12. Scenario 2 is the illustration of the multi-target complex closely spaced and crossing scenario.

Figures 13–16 summarize the quantitative results of Scenario 2. Before step 50, the number of active targets is relatively small and the targets are well separated, so the performance difference among the filters is limited. After step 52, frequent close-range crossings and local aggregations occur, and the performance gap becomes more evident. The total GOSPA and missed-detection components show that EDM-PMBM maintains

lower error during the dense interaction intervals, whereas the compared filters suffer from larger error increases caused by target confusion, erroneous merging, or missed detections.

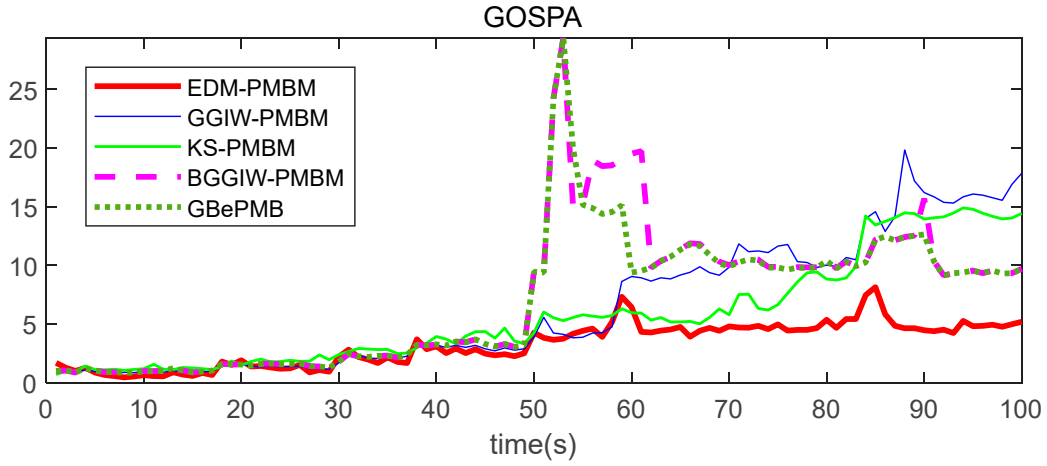


Figure 13. GOSPA error of EDM-PMBM, GGIW-PMBM, KS-PMBM, BGGIW-PMBM, and GBePMB in Scenario 2.

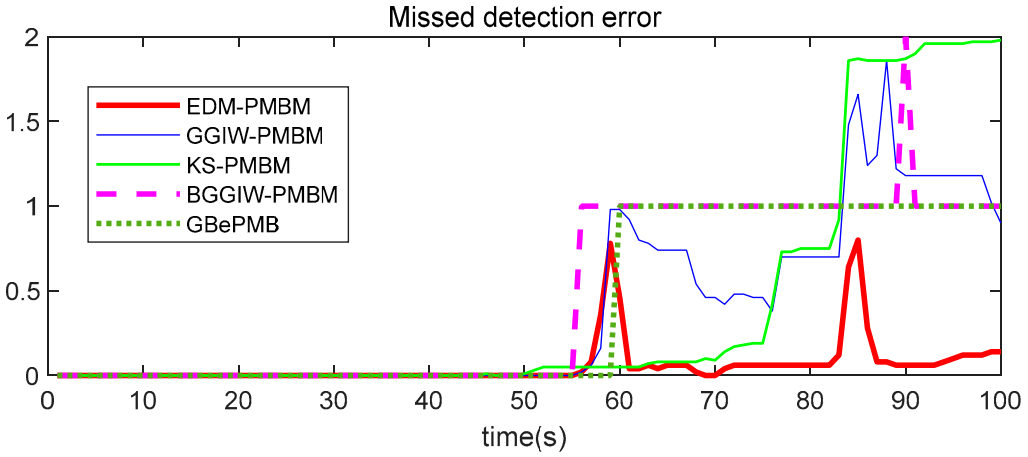


Figure 14. Missed-detection error of EDM-PMBM, GGIW-PMBM, KS-PMBM, BGGIW-PMBM, and GBePMB filters in Scenario 2.

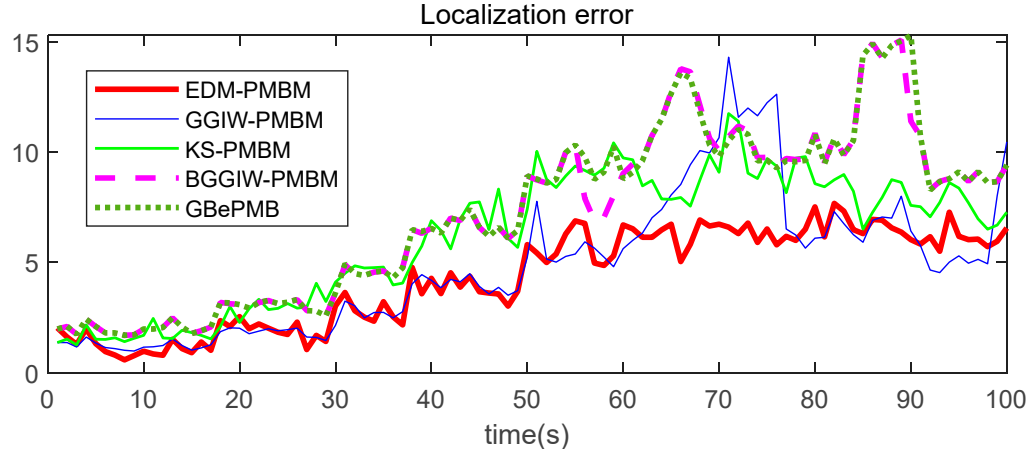


Figure 15. Localization error of EDM-PMBM, GGIW-PMBM, KS-PMBM, BGGIW-PMBM, and GBePMB filters in Scenario 2.

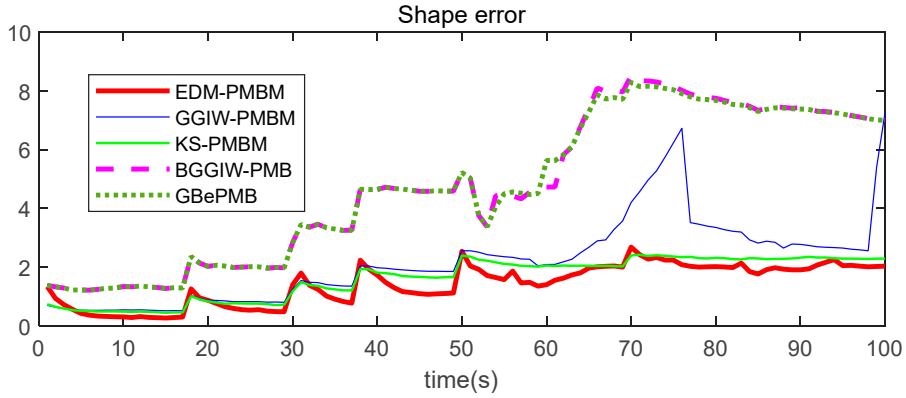


Figure 16. Shape error of EDM-PMBM, GGIW-PMBM, KS-PMBM, BGGIW-PMBM, and GBePMB in Scenario 2.

Figure 13 compares the total GOSPA errors. Before step 50, errors among filters are small due to few targets and large separations. After step 52, as frequent close-range crossings begin, performance diverges. The EDM-PMBM consistently stays at a low level; although fluctuations appear during the densest aggregation, its overall increase is much smaller than that of other filters.

The localization and shape-error results further confirm this trend. EDM-PMBM keeps a smoother localization error and a lower shape error in the mid-to-late stage. This improvement comes from the EDM-domain likelihood, which provides additional contour-dependent discrimination beyond the ordinary ellipsoidal random-matrix statistics.

The decrease in localization or shape error of a baseline filter after severe missed detections should not be regarded as a real performance improvement, because lost targets no longer contribute to the corresponding error accumulation. Therefore, the total GOSPA, missed-detection error, localization error, and shape error should be considered jointly. Overall, Scenario 2 shows that EDM-PMBM is more robust in high-density multi-target crossing conditions.

Figure 17 reports the time cost of the filters compared in Scenario 2. In this scenario, the runtime is closely related to the number of maintained targets and the ambiguity of measurement partitioning. During the middle interval, GGIW-PMBM has a relatively low time cost because it loses one target in the close-crossing process. After the target is lost, fewer Bernoulli components and feasible target-measurement associations are maintained, so fewer likelihood evaluations and global-hypothesis comparisons are required. Therefore, the reduced time cost of GGIW-PMBM in this interval should not be interpreted as better computational efficiency alone, but should be considered together with the GOSPA result, where the missed-target penalty increases.

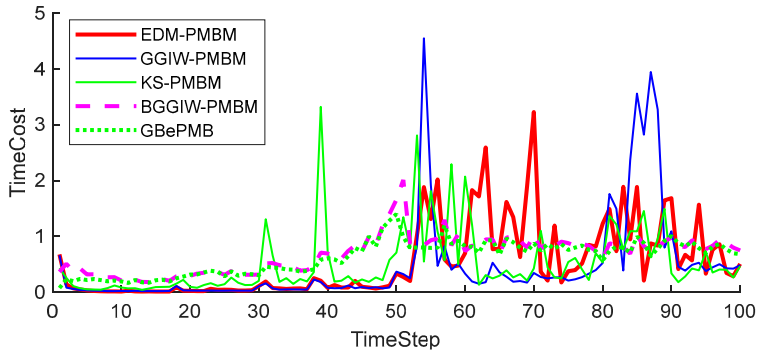


Figure 17. TimeCost for the EDM-PMBM, GGIW-PMBM, KS-PMBM, BGGIW-PMBM, and GBePMB filters in Scenario 2.

In contrast, EDM-PMBM maintains the targets more stably in this scenario. As a result, more valid target hypotheses are preserved, and more target-measurement associations are evaluated. This may lead to a higher time cost than a filter that has already lost a target, but it also corresponds to better track continuity and lower GOSPA error.

6. Conclusions

This paper proposed an extension-difference-mapping-based PMBM filter for non-ellipsoidal extended target tracking. The method represents the irregular target contour by a Fourier-based radial function and constructs a direction-dependent EDM scaling function between the irregular contour and its ellipsoidal baseline. By mapping target-associated measurements into the EDM domain, the proposed method introduces non-ellipsoidal shape differences into likelihood evaluation and data association while retaining the recursive structure of the GGIW-PMBM filter.

Simulation results in two close-crossing scenarios showed that EDM-PMBM reduces the total GOSPA error, missed detections, localization error, and shape error compared with the baseline filters. The results indicate that the EDM-domain likelihood provides additional shape discrimination when multiple extended targets have similar ellipsoidal extents but different local contour structures.

The current method still has several limitations. First, the EDM mapping relies on a radial contour representation and is most suitable for targets that can be approximated as star-convex with respect to the estimated center. Strongly non-star-convex contours or multiple boundary intersections along the same ray may reduce the accuracy of the radial approximation. Second, the current simulations use a simplified measurement model. Sparse measurements, structured clutter, persistent occlusion, and realistic radar reflectivity may affect contour reconstruction and EDM likelihood evaluation. Future work will consider more general contour representations, more realistic sensing models.

Author Contributions: Conceptualization, Y.X. and P.L.; Methodology, Y.X. and P.L.; Software, Y.X. and P.L.; Validation, Y.X., P.L. and Y.S.; Formal analysis, Y.X.; Investigation, Y.X. and W.G.; Resources, Y.S. and J.D.; Data curation, P.L.; Writing—original draft, Y.X.; Writing—review & editing, Y.X. and P.L.; Visualization, Y.X., W.W. and Y.S.; Supervision, Y.X. and W.W.; Project administration, Y.X. and W.W.; Funding acquisition, Y.X. and P.L. All authors have read and agreed to the published version of the manuscript.

Funding: This research received no external funding.

Data Availability Statement: The code for this work has been open-sourced on GitHub. Readers can access the complete implementation of the EDM-PMBM filter and its corresponding parameters at the repository https://github.com/OmegaEta/EDM (accessed on 22 June 2026). This repository not only contains the EDM-PMBM filter, but also provides full code implementations of four comparison filters: GGIW-PMBM, KS-PMBM, BGGIW-PMBM, and GBePMB.

Conflicts of Interest: The authors declare no conflict of interest.

References

1. Vo, B.N.; Mallick, M.; Bar-Shalom, Y.; Coraluppi, S.; Osborne, R.; Mahler, R.; Vo, B.T. Multitarget tracking. In *Wiley Encyclopedia of Electrical and Electronics Engineering*; Wiley: Hoboken, NJ, USA, 2015.
2. Bouraya, S.; Belangour, A. Multi object tracking. In Proceedings of the Thirteenth International Conference on Digital Image Processing (ICDIP), Singapore, 20–23 May 2021; pp. 142–152.
3. Mahler, R. *Statistical Multisource-Multitarget Information Fusion*; Artech House: Norwell, MA, USA, 2007.
4. Mahler, R. *Advances in Statistical Multisource Multitarget Information Fusion*; Academic: Norwell, MA, USA, 2014.
5. Lindenmaier, L.; Aradi, S.; Bécsi, T.; Törő, O.; Gáspár, P. GM-PHD filter based sensor data fusion for automotive frontal perception system. *IEEE Trans. Veh. Technol.* **2022**, *71*, 7215–7229. [CrossRef]

6. Xu, C.; Yang, L.; Li, Y.; Sun, H.; Wang, H.; Gao, X. A novel SMC-PHD filter for multi-target tracking without clustering. *Digit. Signal Process.* **2022**, *71*, 102113.
7. Li, T.; Hlawatsch, F. A distributed particle PHD filter using arithmetic-average fusion of Gaussian mixture parameters. *Inf. Fusion* **2021**, *73*, 111–124. [CrossRef]
8. Mahler, R. PHD filters of higher order in target number. *IEEE Trans. Aerosp. Electron. Syst.* **2007**, *43*, 1523–1543. [CrossRef]
9. Reuter, S.; Vo, B.T.; Vo, B.N.; Dietmayer, K. The labeled multi-Bernoulli filter. *IEEE Trans. Signal Process.* **2014**, *62*, 3246–3260. [CrossRef]
10. García-Fernández, Á.F.; Williams, J.L.; Granström, K.; Svensson, L. Poisson multi-Bernoulli mixture filter: Direct derivation and implementation. *IEEE Trans. Aerosp. Electron. Syst.* **2018**, *54*, 1883–1901. [CrossRef]
11. Smith, J.; Particke, F.; Hiller, M.; Thielecke, J. Systematic analysis of the PMBM, PHD, JPDA and GNN multi-target tracking filters. In Proceedings of the 2019 22th International Conference on Information Fusion (FUSION), Ottawa, ON, Canada, 2–5 July 2019; pp. 1–8.
12. Li, G.; Li, G.; He, Y. PMBM-based unresolved-group object tracking. *IEEE Trans. Aerosp. Electron. Syst.* **2024**, *60*, 4229–4240.
13. Ge, Y.; Kaltiokallio, O.; Xia, Y.; García-Fernández, Á.F.; Kim, H.; Talvitie, J.; Valkama, M.; Wymeersch, H.; Svensson, L. Batch SLAM with PMBM data association sampling and graph-based optimization. *IEEE Trans. Signal Process.* **2025**, *73*, 2139–2153. [CrossRef]
14. Xue, X.; Wei, D.; Huang, S. PETC-EM-PMBM filter for tracking point and extended targets with type conversion. *IEEE Trans. Aerosp. Electron. Syst.* **2024**, *61*, 2235–2249.
15. Chen, L.; Gao, L.; Xia, Y.; Yang, C.; Shang, Z.; Su, Z.; Yuan, T.; Wei, P. Possibility PMBM filter for robust multi-target tracking. *Signal Process.* **2026**, *243*, 110483. [CrossRef]
16. Koch, J.W. Bayesian approach to extended object and cluster tracking using random matrices. *IEEE Trans. Aerosp. Electron. Syst.* **2008**, *44*, 1042–1059. [CrossRef]
17. Lan, J. Extended object tracking using random matrix with extension-dependent measurement numbers. *IEEE Trans. Aerosp. Electron. Syst.* **2023**, *59*, 4464–4477. [CrossRef]
18. Granström, K.; Natale, A.; Braca, P.; Ludeno, G.; Serafino, F. Gamma Gaussian inverse Wishart probability hypothesis density for extended target tracking using X-band marine radar data. *IEEE Trans. Geosci. Remote Sens.* **2015**, *53*, 6617–6631. [CrossRef]
19. Granström, K.; Orguner, U. New prediction for extended targets with random matrices. *IEEE Trans. Aerosp. Electron. Syst.* **2014**, *50*, 1577–1589. [CrossRef]
20. Li, M.; Lan, J.; Li, X.R. Tracking of extended object using random triangle model. *IEEE Trans. Aerosp. Electron. Syst.* **2024**, *61*, 2926–2940. [CrossRef]
21. Granström, K.; Willett, P.; Bar-Shalom, Y. An extended target tracking model with multiple random matrices and unified kinematics. In Proceedings of the 2015 18th International Conference on Information Fusion (Fusion), Washington, DC, USA, 6–9 July 2015; pp. 1007–1014.
22. Xue, X.; Huang, S.; Wei, D. Adaptive tracking of non-ellipsoidal extended target with varying number of sub-objects based on variational Bayesian. *Digit. Signal Process.* **2023**, *142*, 104214.
23. Baum, M.; Hanebeck, U.D. Extended object tracking with random hypersurface models. *IEEE Trans. Aerosp. Electron. Syst.* **2014**, *50*, 149–159. [CrossRef]
24. Yang, J.; Li, P.; Li, Z.; Yang, L. Multiple extended target tracking method based on Gaussian surface matrix. *J. Syst. Eng. Electron.* **2016**, *27*, 279–289.
25. Li, P.; Ge, H.W.; Yang, J.L.; Wang, W. Modified Gaussian inverse Wishart PHD filter for tracking multiple non-ellipsoidal extended targets. *Signal Process.* **2018**, *150*, 191–203. [CrossRef]

Disclaimer/Publisher's Note: The statements, opinions and data contained in all publications are solely those of the individual author(s) and contributor(s) and not of MDPI and/or the editor(s). MDPI and/or the editor(s) disclaim responsibility for any injury to people or property resulting from any ideas, methods, instructions or products referred to in the content.